5-1-2020

Finite element analysis of extruded AA6061-T6 mechanical connection in low-cycle fatigue

Nolan Hoffman

Finite element analysis of extruded AA6061-T6 mechanical connection in low-cycle fatigue

By

Nolan Hoffman

Approved by:

Youssef Hammi (Major Professor)
Timothy W. Rushing
Matthew W. Priddy
Wilburn Whittington
Yucheng Liu (Graduate Coordinator)
Jason M. Keith (Dean, Bagley College of Engineering)

A Master's Thesis
Submitted to the Faculty of
Mississippi State University
in Partial Fulfillment of the Requirements
for the Degree of Master of Science
in Mechanical Engineering
in the Department of Mechanical Engineering

Mississippi State, Mississippi

May 2020

Name: Nolan Hoffman

Date of Degree: May 1, 2020

Institution: Mississippi State University

Major Field: Mechanical Engineering

Major Professor: Youssef Hammi

Title of Study: Finite element analysis of extruded AA6061-T6 mechanical connection in low-cycle fatigue

Pages in Study 70

Candidate for Degree of Master of Science

The low-cycle fatigue (LCF) life of the extruded aluminum alloy 6061-T6 (AA6061-T6) AM2 matting connection system was analyzed through 3D finite element modeling in conjunction with the plasticity-damage (DMG) and multi-stage fatigue (MSF) material models. The connection was modeled in ABAQUS Explicit based on the real-world boundary conditions of AM2 matting. The DMG-MSF user-defined material model characterized the low-cycle fatigue damage evolution within the microstructure of the extruded AA6061-T6 connection and utilized the maximum effective strain amplitude to predict the life of each stage of the fatigue process. It was determined that a constant displacement range of 15.17 mm generated an effective strain amplitude of 6.8E-03 mm/mm and a predicted total fatigue life within 1% to the laboratory- and full-scale data at approximately 1,122 cycles. The LCF characterization of the connection system allows for a significant reduction in laboratory- and full-scale testing for future design improvements.

ACKNOWLEDGEMENTS

The author would like to acknowledge Mississippi State University and the U.S. Army Engineer Research and Development Center for providing the resources necessary to pursue this solution.

More specifically, the author would like to thank Dr. Youssef Hammi, Dr. Tim Rushing, Dr. Matthew Priddy, and Dr. Wil Whittington for the guidance, motivation, and insight to make the completion of this thesis possible.

TABLE OF CONTENTS

LIST OF TABLES

LIST OF FIGURES

CHAPTER I

INTRODUCTION

Background

Aluminum alloy 6061 (AA6061) has been utilized for structural applications in the transportation industry for many years due to its high strength-to-weight ratio, manufacturability, and corrosion resistance [1-5]. Additionally, AA6061 has been used extensively by the U.S. Department of Defense (DoD) to create temporary airfield surfacing systems since the 1960s [6-9]. Other materials such as steels, plastics, and composites have been used and are still being used for a variety of matting applications, however, extruded AA6061 is the primary material for U.S. military expeditionary airfield surfacing. The most commonly used expeditionary airfield surfacing system is referred to as AM2 matting. Ever since its introduction, AM2 matting has been fabricated from extruded AA6061-T6. AM2 matting is produced in three separate pieces. The three pieces include a multi-void hollow-core extrusion with tongue and groove connectors, an extruded overlap/underlap locking joint, and an extruded insert that is fit into the ends of the hollow core and welded in place prior to welding the locking connectors.

Historically, AM2 matting is assembled in an array and utilized as an expeditionary airfield surface to support fighter and cargo aircraft over graded but unimproved soils, as shown in Figure 1. Therefore, the mats are the primary support structure for the aircraft since unimproved subgrades are typically weak. The performance of AM2 matting has been quantified at the U.S. Army Engineer Research and Development Center (ERDC) in Vicksburg, MS through full-scale testing

over subgrade strengths of 6%, 10%, 15%, 25%, and 100% California Bearing Ratio (CBR) with simulated F-15E and C-17 traffic. This work is focused on the F-15E related data over the 6% CBR subgrade.

Figure 1 Photograph of AM2 matting installation

The F-15E traffic was applied with a single F-15E wheel and tire inflated to 2,240 kPa (325 psi). The load on the single tire was 157 kN (35,235 lbf), which generated a contact area of 706 cm^2 (109.5 $in.^2$). The wheel traveled along 5 five parallel lanes that were 23 cm (9 in.) apart, which created a total traffic width of 115 cm (45 in.). The five lanes were traversed in a pattern that allowed the three center lanes to receive twice as much traffic as the outer lanes to generate a simplified, normal distribution. The distributed traffic pattern allowed the loaded wheel to travel the center lane 4 times for each 16 total passes, which created a pass-to-coverage ratio of 4.

The current minimum subgrade strength requirement for AM2 matting is quantified as a CBR of 6%. The current performance requirement for AM2 matting is to sustain 1,500 passes of

a fully-loaded F-15E or C-17 aircraft traffic when placed over a 6% CBR subgrade in a brickwork pattern; where failure is considered to be failure of 10% of the matting surface area. AM2 failures typically occur within the locking connection (shown in Figure 2) on the short edge of the matting, which is parallel to the direction of traffic [7-8]. Therefore, it is reasonable to assume that the connectors begin failing prior to the completion of the 1,500 passes. Results from full-scale testing at the U.S. Army ERDC [8] showed that the first panel failure occurred after approximately 984 passes while the 10% failure criterion was reached at 1,395 passes, creating an average of 1,190 passes. Additionally, it was determined that the number of cycles to failure of the connection was correlated directly to the plastic deformation of the subgrade. The matting failures from the full-scale evaluations shifted from end connector failures to internal core failures as the subgrade strength increased.

Figure 2 Photograph of the AM2 locking connection

Rushing et al. [7] evaluated the AM2 locking connection in a laboratory-scale environment to understand the performance of the joint without the expense of the constructing an entire test section and matting array. A laboratory procedure was developed to simulate the joint movement seen in full-scale testing, which is shown in Figure 3.

Additionally, to replicate the appropriate range of motion within the connection when the matting wsa trafficked, the vertical displacement of the laboratory specimens was correlated to the deformation of the subgrade measured in full-scale testing, which can be determined by Equation 1. It was noted that the width of the rut formed in the subgrade was based on traffic application, not the strength of the subgrade. Considering that the total span of the laboratory experiment was 62.23 cm (24.5 in.), which was approximately half of the width of the typical rut formed during the full-scale experiments, Equation 1 was multiplied by 0.5 to give an equivalent amount of rotation within the joint. Therefore, Equation 2 calculates the displacement applied to the laboratory specimens per cycle. Where δ_s is the subgrade displacement from its original level, P_n is the number of passes, and CBR is the strength of the subgrade beneath the matting in terms of %.

It was learned from the laboratory experiments [7] that failures were only replicated accurately when the joint was loaded on the underlapping side exclusively, while restraining the overlapping side rigidly. When the connection was is loaded from the overlapping side, the joint engages fully along its length and the stress is transferred through the teeth without engaging the locking bar. When the joint is loaded on the underlapping side, however, the large tolerances built into the connection for assembly allow the joint to separate transfer the load through the locking bar over a much smaller area. A representation of the connection engagement modes is shown in Figure 4.

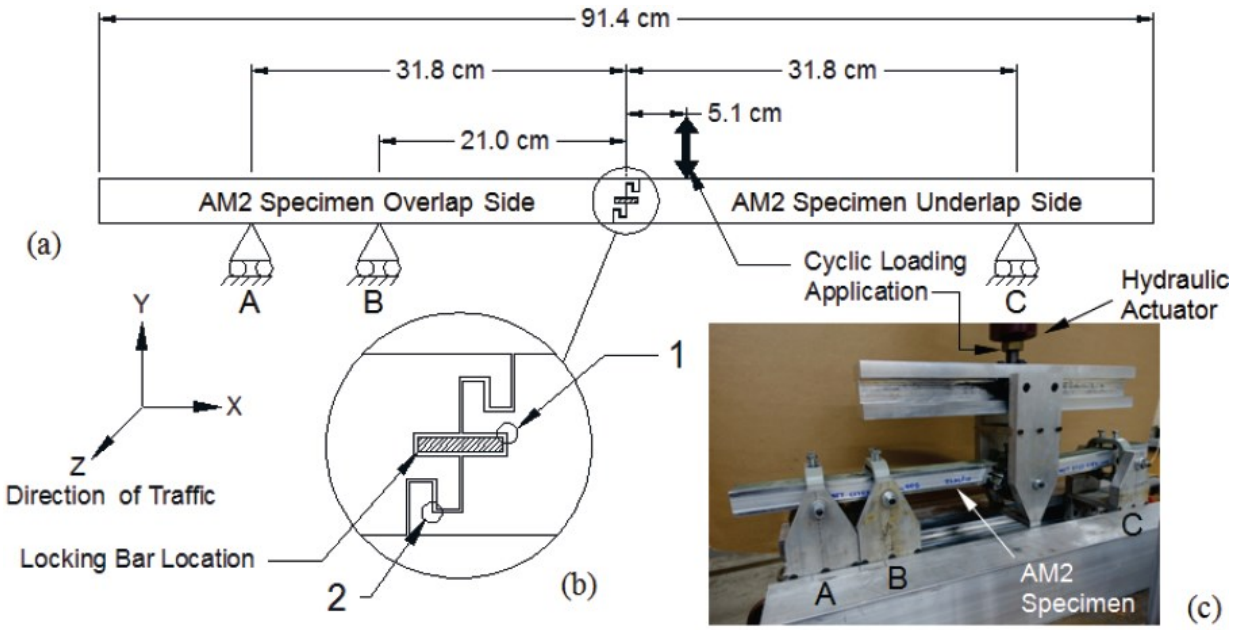

Figure 3 Schematic of the testing boundary conditions for the AM2 connection

Section a) shows the laboratory testing boundary conditions, b) depicts the two primary failure locations within the connection, and c) is a picture of the actual setup used by Rushing et al. [7,8]

$$\delta_s = log_{10}P_n * 1.64 * CBR^{-0.61} \quad (1)$$

$$\delta_s = log_{10}P_n * 0.82 * CBR^{-0.61} \quad (2)$$

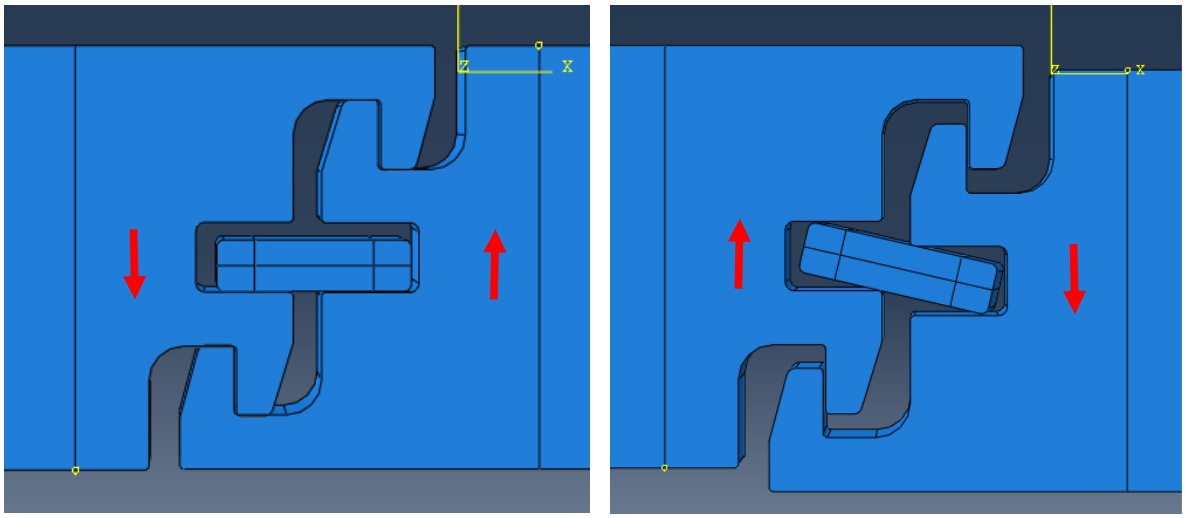

(a) (b)

Figure 4 Schematic of the overlapping AM2 connection under two loading conditions

Condition a) was loaded on the overlapping side and condition b) was loaded on the underlapping side

Reported failures were consistent with the full-scale data showing a propagated crack through the upper tooth of the underlap locking connector, as shown in Figure 5. The data revealed that the average number of cycles to failure for the locking connection was 1,132 cycles. Considering that failure occurs below 1,500 cycles, the connection is undergoing low-cycle fatigue (LCF).

Fatigue is an important failure criterial that is defined as repeated loading cycles that cause damage to accumulate within the material, effectively weakening or creating a finite lifespan [10]. Extensive testing and characterization are required in order to understand the intrinsic and extrinsic factors on material properties of a metal in fatigue. Fatigue of metals consists of four main stages: incubation (INC), microstructurally small crack (MSC), physically small crack (PSC), and long crack (LC). While MSC and PSC are sometimes combined for simplicity, INC can be broken down

into three sub-stages including void nucleation, growth, and coalescence [5]. Understanding the fatigue properties of extruded AA6061-T6 is crucial to understanding the performance of AM2 matting connection and has the potential to reduce laboratory- and full-scale prototyping efforts for design improvements.

(a) (b)

Figure 5 Photographs of the AM2 connection and failure location

Section a) shows the typical crack location circled and section b) shows the typical failure mode shown [6,7]

CHAPTER II

LITERATURE REVIEW

Mechanical characterization

Extrusion is the manufacturing process where a billet of material is forced through a small opening in a die to produce a near net shape part. A significant amount of pressure is applied to the material forcing the material to flow through the die. As a result, the material undergoes a large amount of plastic deformation. The large amounts of plastic deformation affects the microstructure of the metal resulting in different properties than wrought AA6061. Therefore, the properties of extruded AA6061 need to be quantified to have an accurate representation of the material being used to produce AM2 matting. The chemical composition (Wt. %) of AA6061-T6 is shown in Table 1 [2, 4]. Even though the base material composition is unaltered during extrusions, it is critical to the strength of an alloy [11], the aging condition contributes significantly to the strength as well [12].

Dorward and Bouvier [11] analyzed the effect of composition on the strength, ductility, and toughness of AA6061. The authors analyzed variations of magnesium and silicon content within the material. Peak yield strength was greatly affected by composition, with approximately a 100 MPa difference between the strongest and weakest alloys. Peak strength increased by approximately 5 MPa with each 0.1% increase in Mg_2Si. Specimens with lean and nominal chemistries of silicon and magnesium showed the best combination of strength and toughness. The authors noted that strength increased with aging time for all of the variations tested; however,

elongation decreased with aging time. Therefore, the tensile and toughness properties of AA6061-T6 can vary based on both the exact composition of the alloy and the aging process.

Table 1 Chemical composition of AA6061-T6 in wt.%

Element	Mg	Si	Cu	Mn	Fe	Cr	Zn	Al
Min.	0.80	0.40	0.15	--	--	0.04	--	Bal.
Max.	1.20	0.80	0.40	0.15	0.7	0.35	0.25	Bal.

[2,4]

Abood et al. [2] compared the effect of heat treatment on the mechanical properties of AA6061 in three different conditions. The three conditions were annealed (O), T4, and T651. Monotonic stress-strain data can be seen in Table 2. As expected, the yield strength and ultimate strength increased as the aging condition increased. Additionally, the authors measured elongation at 13%, 19%, and 28% via tensile testing for the T651, T4, and O conditions, respectively. The strain hardening exponent and strength coefficient of the three aging conditions are also listed in Table 2. The main takeaway from this work was that as the treatment increased, the yield strength increased, and the elongation decreased. The decreased ductility due to an increase in hardness is consistent with [11].

Ozturk et al. [12] investigated the influence of the T6 aging treatment specifically on the mechanical properties of AA6061. The T6 condition is a very common method to increase the strength of AA6061. A solution heat treatment occurs at 500 C to obtain the supersaturated α solid solution. Then, artificial aging is performed by heating the alloy to 200 C to allow for precipitation of various phases. The hardness and strength of AA6061 depends on the precipitate type, density and size [13]. The authors determined that peak aging requires a dense population of β needle-shaped precipitates aligned in the <1 0 0> direction to block dislocation movement. The peak aged

condition, which occurs after 200 minutes of aging at 200 C, showed an increase of 73% over the material without any heat treatment. As expected, it was noted that ductility is inversely proportional to the strength. The total elongation for the peak aged material was 13.2% while the non-treated material measured an elongation of 24.6%. Due to the heat treatment process, the presence of β" precipitates within the microstructure led to drastic changes in the mechanical properties, such as increasing the yield strength and hardness values.

In summary, the microstructure of AA6061 changes with the chemical composition, the manufacturing process, and the ageing process. Takahashi et al. [14] and McCullough [15] characterized the microstructure of extruded AA6061-T6. Figure 6 and Figure 7 show the highly textured microstructure with grains that are elongated in the extrusion direction. The grains are oriented in the <111> and the <100> direction. The fine, needle-like precipitates in Figure 6d are oriented in the <100> direction and ranged from 20-100 nm in length. Based on the findings from [5, 14-15], it was confirmed that the extruded AA6061-T6 has a unique microstructure due to the processing methods.

Abood et al. [2], Brammer et al. [4], McCullough et al. [5], Mirza et al. [16], and Wong et al. [21] quantified the monotonic tensile properties of extruded AA6061-T6. The uniaxial results from the material can be seen in Table 2. Overall, the alloys exhibited similar yield and tensile strengths. As expected, it can be seen in Table 2 that the lesser-aged conditions have lower strengths but higher elongation. The variation in tensile properties for the materials with the same aging conditions may be a result of slightly different chemical composition or heat treatment process.

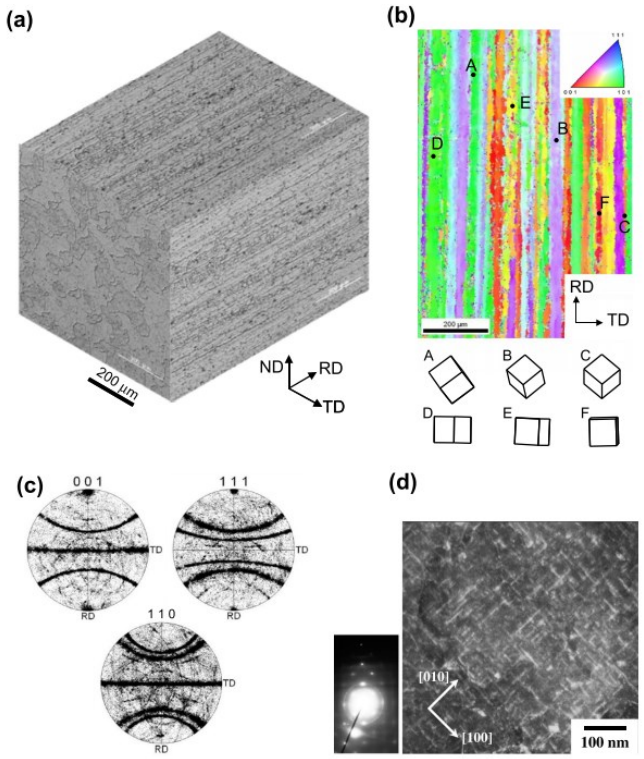

Figure 6 Microstructural analysis of extruded AA6061-T6

The analysis shows a) a 3D stitched view from optical micrographs, b) an inverse pole figure color map of the surface, c) pole figures captured from b), and d) a transmission-electron microscopy image of needle-shaped precipitates within the specimen [14]

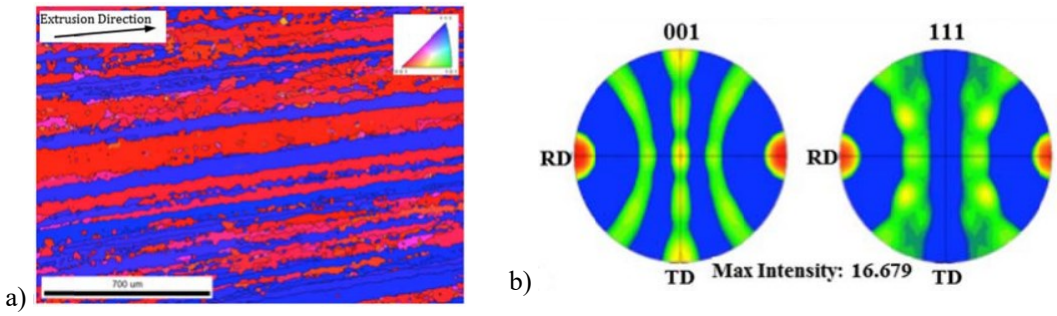

Figure 7 EBSD images of extruded AA6061-T6

Electron backscatter diffraction images of extruded AA6061-T6 with a) inverse pole figure map and b) pole figures of the specimens in the extrusion direction [15]

Table 2 Monotonic tensile properties of extruded AA6061

Material	Elastic Modulus (GPa)	Yield Strength (MPa)	Ult. Tensile Strength (MPa)	Elong-ation (%)	Monotonic Strength Coefficient *K*, (MPa)	Strain-Hardening Exponent, *n*
AA6061-T651 [2]	--	300.0	338.0	13.0	480.0	0.052
AA6061-T4 [2]	--	262.0	307.0	19.0	400.0	0.069
AA6061-O [2]	--	73.0	127.0	28.0	110.0	0.158
AA6061-T6 [4]	67.8	296.0	320.0	--	178.0	0.360
AA6061-T6 [5]	66.4	304.4	320.8	20.0	377.4	0.039
AA6061-T6 Custom [5]	67.5	270.3	292.5	22.7	355.4	0.050
AA6061-T6 [16]	66.9	297.0	319.0	21.5	470.0	0.120
AA6061-T6 [21]	69.6	319.9	347.5	11.8	337.2	0.017

Fatigue properties

When a metal undergoes strain-controlled deformation, the elastic strain amplitude dominates when small strains are applied; however, the plastic strain amplitude dominates when large strains are applied [10]. Both the elastic and plastic strain amplitudes contribute to the total fatigue life in the LCF of extruded AA6061-T6. Total fatigue life can be summarized by Equation 3,

$$\frac{\Delta\varepsilon_{tot}}{2} = \frac{\Delta\varepsilon_e}{2} + \frac{\Delta\varepsilon_p}{2} \quad (3)$$

where $\frac{\Delta\varepsilon_{tot}}{2}$ is the total strain amplitude, $\frac{\Delta\varepsilon_e}{2}$ is the elastic strain amplitude, and $\frac{\Delta\varepsilon_p}{2}$ is the plastic strain amplitude. The elastic strain amplitude can be broken down using Basquin's equation [17] into Equation 4,

$$\frac{\Delta\varepsilon_e}{2} = \frac{\sigma_f'}{E}\left(2N_f\right)^b \tag{4}$$

where E is the elastic modulus, σ_f' is the fatigue strength coefficient, b is the fatigue strength exponent, and $2N_f$ is the number of reversals to failure. The Coffin-Manson relationship [18-19] can be used to represent the plastic strain amplitude, as shown in Equation 5,

$$\frac{\Delta\varepsilon_p}{2} = \varepsilon_f'\left(2N_f\right)^c \tag{5}$$

where ε_f' is the fatigue ductility coefficient, and c is the fatigue ductility exponent. Brammer et al. [4] combined Equation 3 with the Massing's Hypothesis and applied it to the branch equation [20] to create an equation for the stabilized hysteresis loop, creating Equation 6,

$$\Delta\varepsilon = \frac{\Delta\sigma}{E} + 2\left(\frac{\Delta\sigma}{2K'}\right)^{\frac{1}{n'}} \tag{6}$$

where K' is the cyclic strength coefficient and n' is the cyclic strain hardening exponent. Equation 4 can be used to predict the cyclic stress-strain response of the material. Therefore, quantifying the parameters from Equations 3-6 allows one to understand the response of AA6061-T6 to fatigue loading. The following works [3, 4, 5, 16, & 21] have quantified the LCF parameters from Equations 3-6.

Badaruddin et al. [3] studied the LCF performance of extruded AA6061-T6 under strain-controlled testing. The results are plotted in Figure 8. All testing was fully-reversed at a strain rate of .004/s over a range of strain amplitudes from 0.5% to 1.3%. The authors found that strain softening occurred at a strain amplitude of 0.7% and below while strain hardening occurred at strain amplitudes of 1.1% and above. Figure 9 shows the strain hardening and softening behavior. The strain softening was attributed to dislocation annihilation because the secondary phase particles (Mg_2Si) cannot restrain the dislocation movement when under compression. The authors attributed the strain hardening to interactions between the secondary phase particles and Mg_2Si precipitates that disrupt the dislocation movement. The authors noted improved fatigue life at the strain rates below .7% due to the lower strength and higher ductility of the material. A minimal amount of the Bauschinger effect was noticed at a strain amplitude of 0.7% (Figure 10a), however, it was not present at an amplitude of 1.3% (Figure 10b). Figure 11 shows that the cyclic stress responses are lower than the monotonic results, which also indicates strain softening. The LCF parameters were recorded in Table 3.

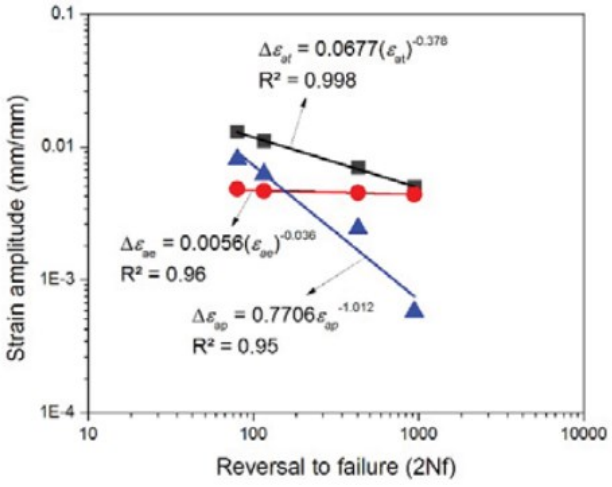

Figure 8 Strain-life plot of extruded AA6061-T6

The plot shows total, elastic, and plastic strain [3]

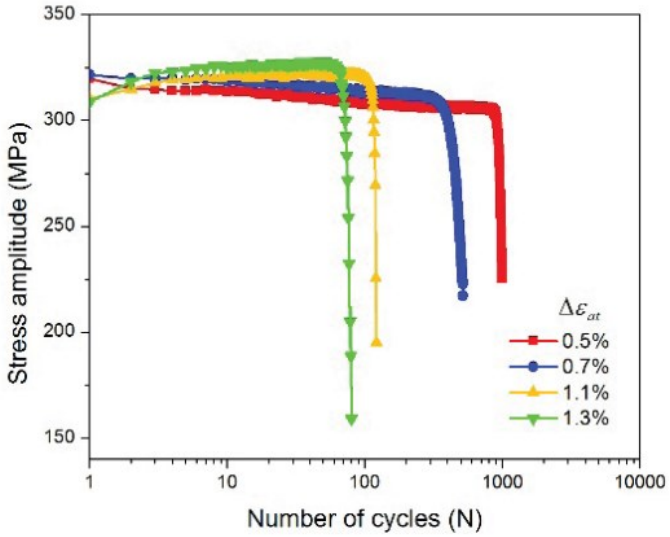

Figure 9 Stress-life plot of AA6061-T6

Stress amplitude versus number of cycles of extruded AA6061-T6 at various strain amplitudes [3]

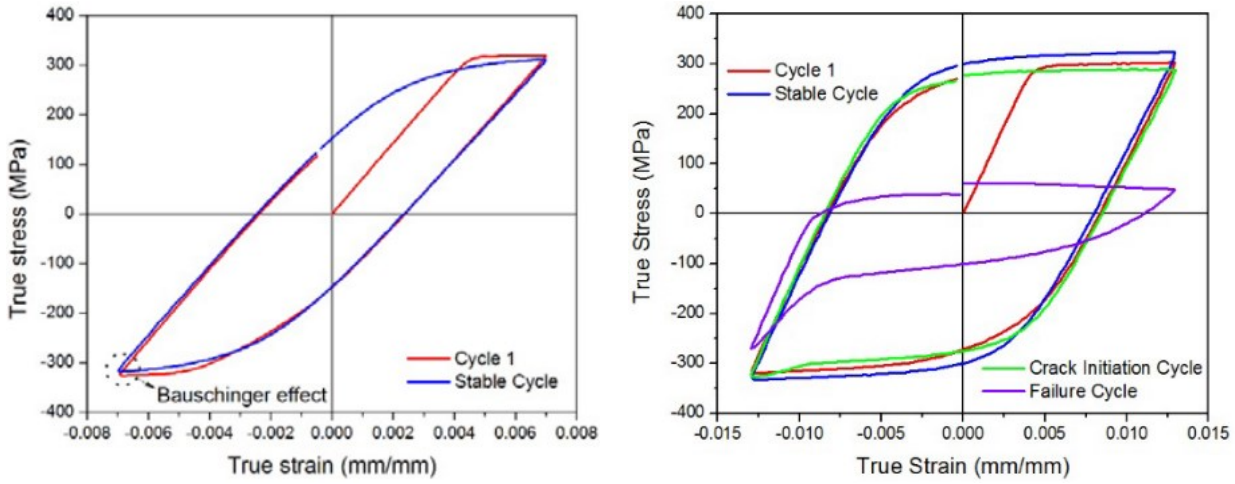

(a) (b)

Figure 10 Hysteresis loops of extruded AA6061-T6

Typical hysteresis loop of extruded AA6061-T6 at a) 0.7% strain amplitude and b) 1.3% strain amplitude [3]

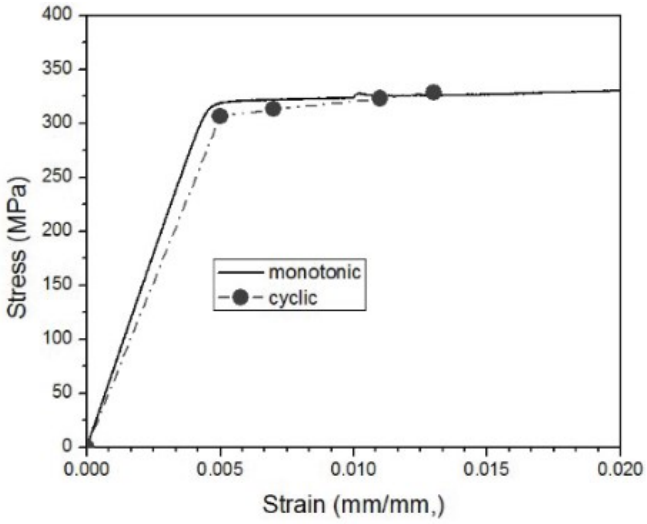

Figure 11 Stress-strain plot for extruded AA6061-T6

Monotonic and cyclic stress-strain curves of extruded AA6061-T6 [3]

Brammer et al. [4] evaluated extruded AA6061-T6 at a variety of strain amplitudes to define the strain-controlled LCF properties. The cyclic tests were run with a frequency of 5 Hz and with strain amplitudes of .002, .003, .004, .005, .006, and .007. The fatigue life results (shown in Figure 12) showed significant strain hardening for strain amplitudes .004 and greater, indicated by the positive slope of the curves, as shown in Figure 13. The stress-strain responses from the first cycle at each strain amplitude shown in Figure 14a were symmetric and did not show signs of the Bauschinger effect. Additionally, Figure 14b shows the hysteresis loops at the half-life for each strain amplitude and only a slight downward shift was observed. The strain-life LCF parameters were tabulated in Table 3.

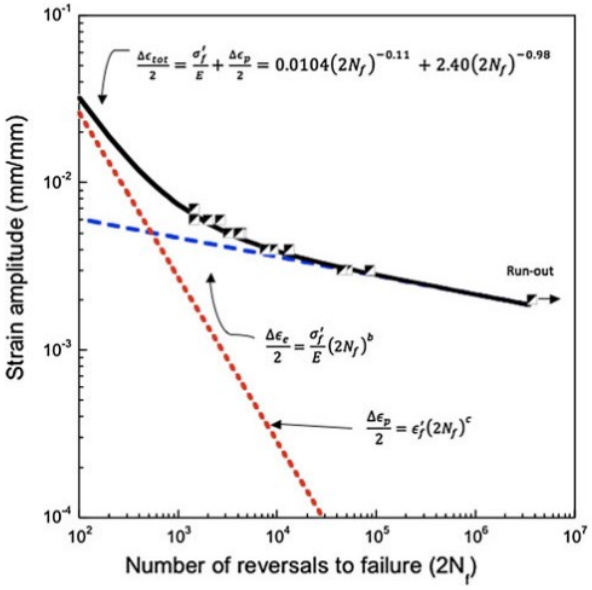

Figure 12 Strain-life plot of extruded AA6061-T6

Curves for the total strain, elastic strain, and plastic strain amplitudes are shown [4]

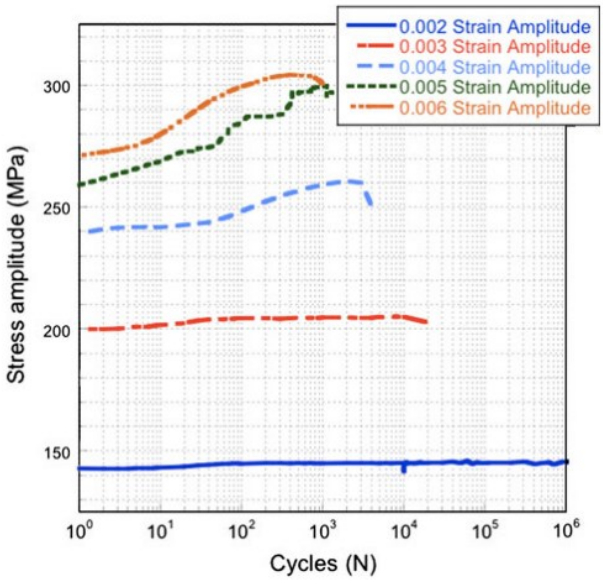

Figure 13 Stress-life plot for extruded AA6061-T6

Stress amplitude versus number of cycles for extruded AA6061-T6 [4]

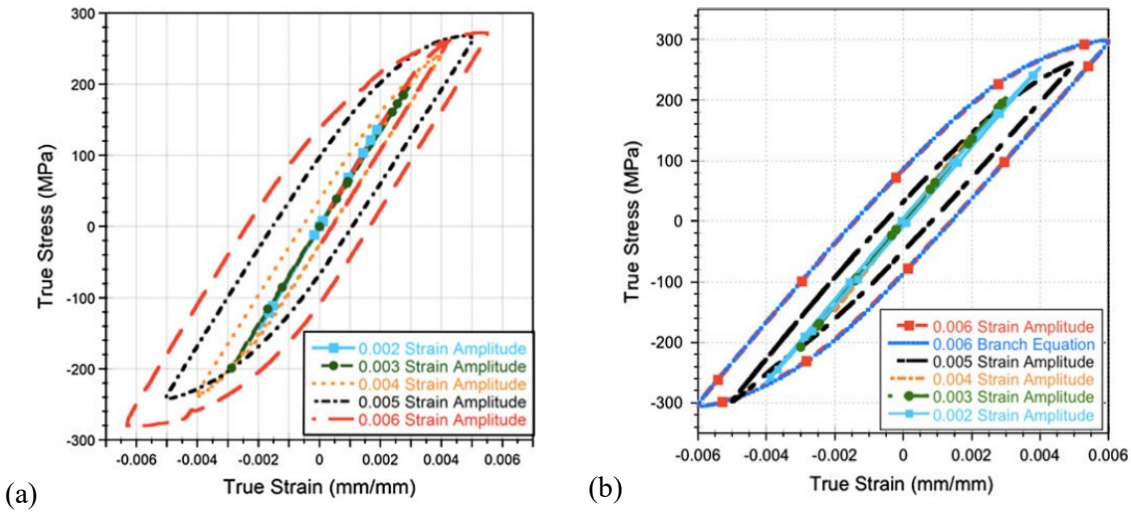

Figure 14 Hysteresis plots for extruded AA6061-T6

Hysteresis loops for a) the first cycle and b) the half-life of extruded AA6061-T6 [4]

McCullough et al. [5] evaluated the fatigue crack nucleation and growth in extruded AA6061 in the T6 condition and a custom annealed condition. The custom condition was evaluated after exposing the AA6061-T6 to an elevated thermal environment. The fully-reversed strain-life fatigue results at a frequency of 5 Hz are shown in Figure 15. A small amount of strain hardening was observed and minimal Bauschinger effects were present in either material, as shown by the first-cycle and half-life hysteresis loops (Figure 16). Even so, almost all of the fatigue tests for both material conditions showed work-softening, as shown by the negative slopes of the curves in Figure 17. In summary, both the T6 and annealed conditions resulted in similar strain-controlled fatigue lives, however, the T6 condition always required more stress to achieve the same strain amplitudes due to its higher yield strength. The authors attributed the reduction in yield strength of the annealed material to the increase in grain size during the slight recrystallization period at elevated temperature. Additionally, the monotonic and cyclic stress-strain response for both

materials are displayed in Figure 18, confirming that more stress is required of the T6 condition in order to reach an equivalent strain as the annealed condition. Also, the lower values for the cyclic results in Figure 18 compared to the monotonic results indicates strain softening behavior. The LCF parameters were recorded in Table 3.

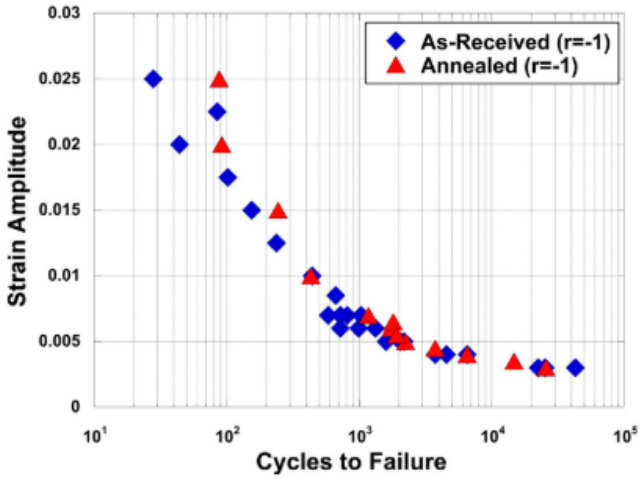

Figure 15 Strain-life plot for extruded AA6061-T6 and heat affect AA6061

Strain-life plot of extruded AA6061-T6 and custom treated AA6061 [5]

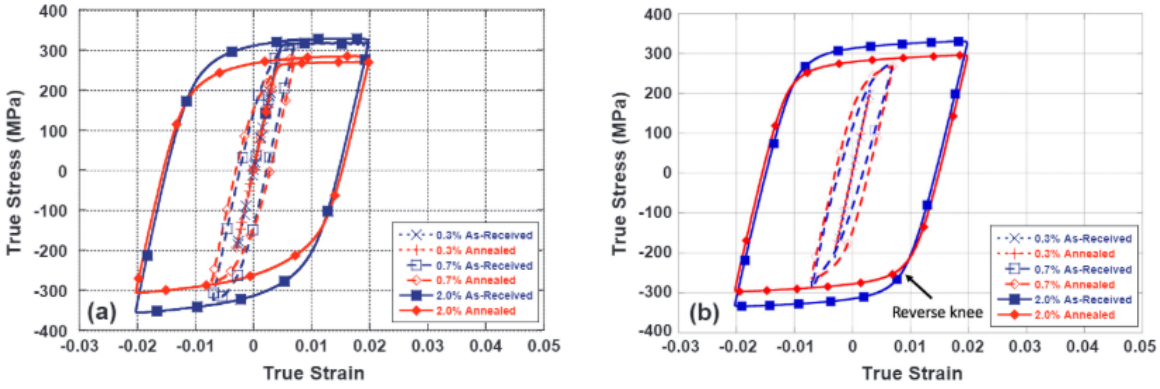

(a) (b)

Figure 16 Hysteresis plots for extruded AA6061-T6 and heat affected AA6061

Typical hysteresis loops for a) the first cycle and b) the half-life of extruded AA6061-T6 and a custom treated AA6061 [5]

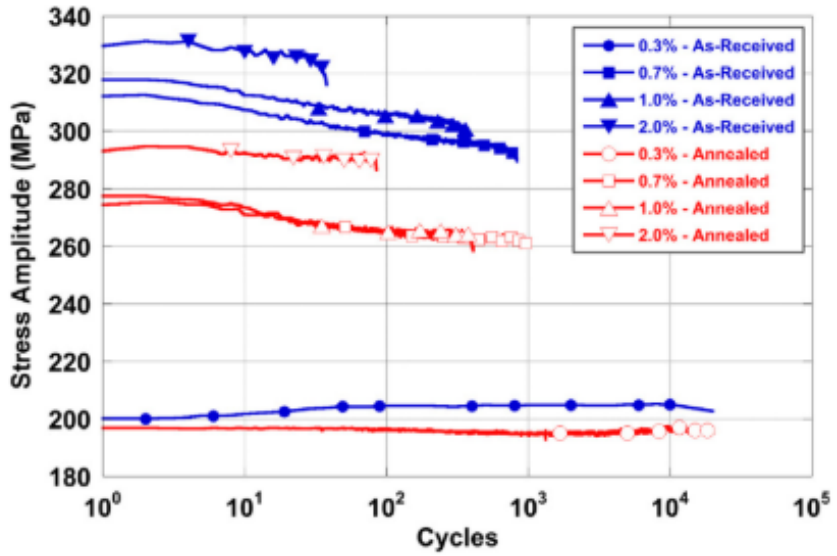

Figure 17 Stress life plot of extruded AA6061-T6 and heat affected AA6061

Stress amplitude versus number of cycles for extruded AA6061-T6 and a custom treated AA6061 [5]

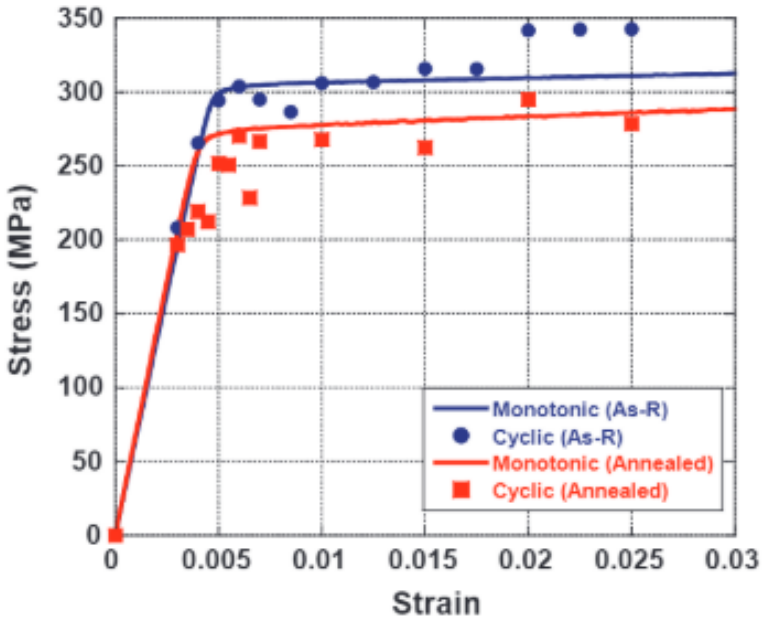

Figure 18 Stress-strain plot for extruded AA6061-T6 and heat affected AA6061

Monotonic and cyclic stress-strain curves for extruded AA6061-T6 and a custom treated AA6061 [5]

Mirza et al. [16] evaluated the strain-controlled LCF behavior of extruded AA6061-T6 under strain amplitudes of 0.4%, 0.6%, 0.8%, 1.0%, and 1.2% at a constant strain rate of $1x10^{-2}$ s^{-1}. The results can be seen in Figure 19a & Figure 19b. The stress-strain responses showed minimal Bauschinger effect, which can be observed in the half-life hysteresis loop at a strain amplitude of 1.2% (Figure 20). Minor cyclic hardening occurred at high strain amplitudes (0.8–1.2%) within the first ten cycles and was followed by cyclic stabilization and then a little softening prior to failure. Figure 21 shows this hardening/softening behavior. The authors reported a longer fatigue life than [4, 21], but is most likely due to higher ductility of the specific material studied. The LCF parameters were recorded in Table 3.

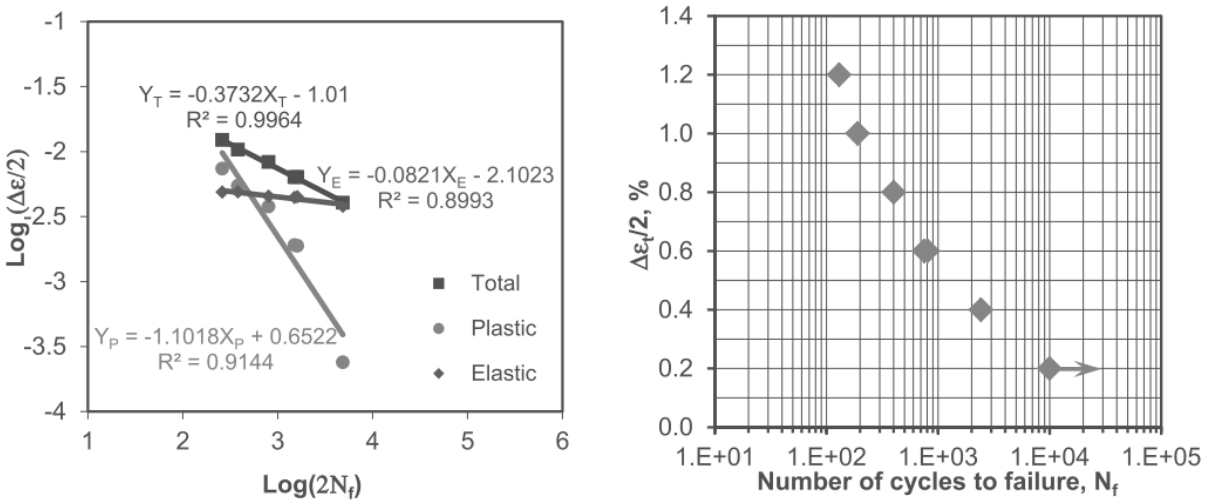

a) b)

Figure 19 Strain life plots of extruded AA6061-T6

The strain-life fatigue plot of extruded AA6061-T6 with a) total, elastic, and plastic strain amplitudes and b) total strain amplitude only [16]

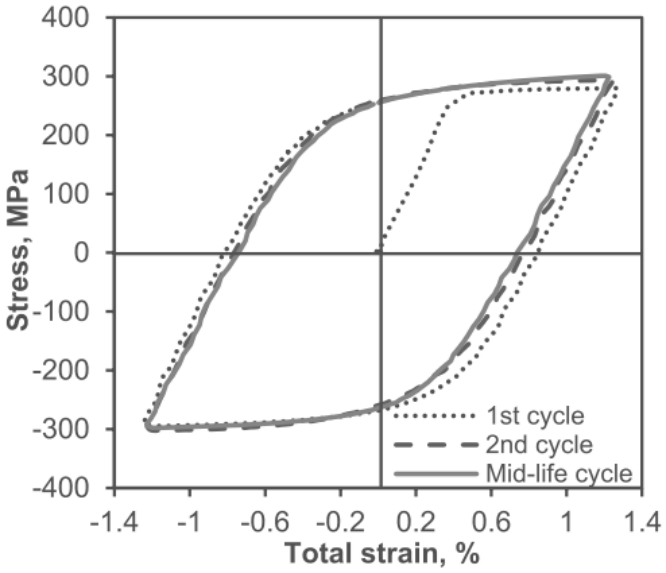

Figure 20 Hysteresis plots of extruded AA6061-T6

Typical hysteresis loop of extruded AA6061-T6 for first, second, and mid-life cycles at a total strain amplitude of 1.2% [16]

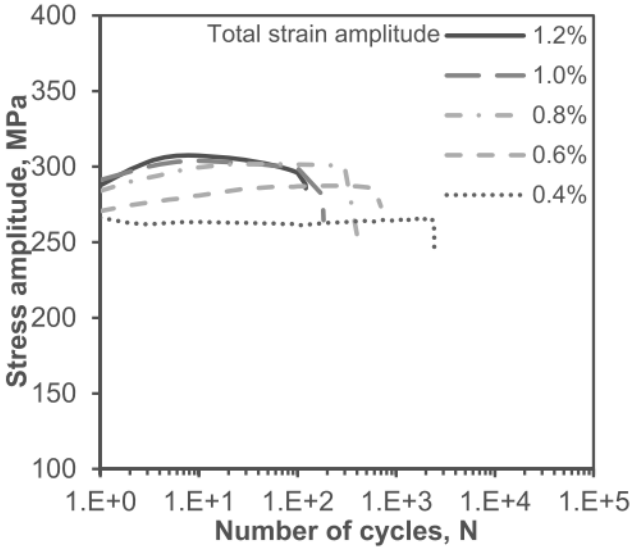

Figure 21 Stress-life plot of extruded AA6061-T6

Stress amplitude versus number of cycles for extruded AA6061-T6 at various strain amplitudes [16]

Wong et al. [21] performed strain-life LCF testing of 3 lots of extruded AA6061-T6. The tests were performed fully-reversed and uniaxial at a strain rate of 0.01 s^{-1}. The material showed slight cyclic hardening, with a 3% increase in the cyclic yield strength over the monotonic yield strength, as shown in Figure 22. The strain-life plot is shown in Figure 23, including the elastic and plastic strain-life curves. The LCF parameters were calculated and listed in Table 3.

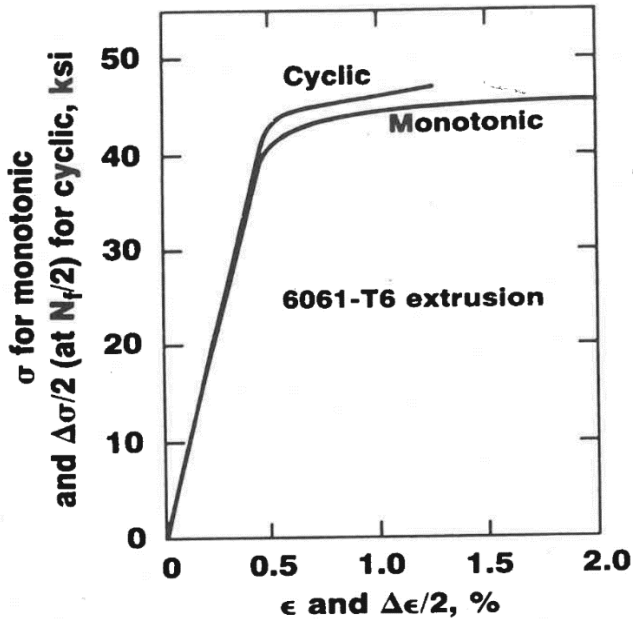

Figure 22 Stress-strain plot for extruded AA6061-T6

Monotonic and cyclic stress-strain curves for extruded AA6061-T6 [21]

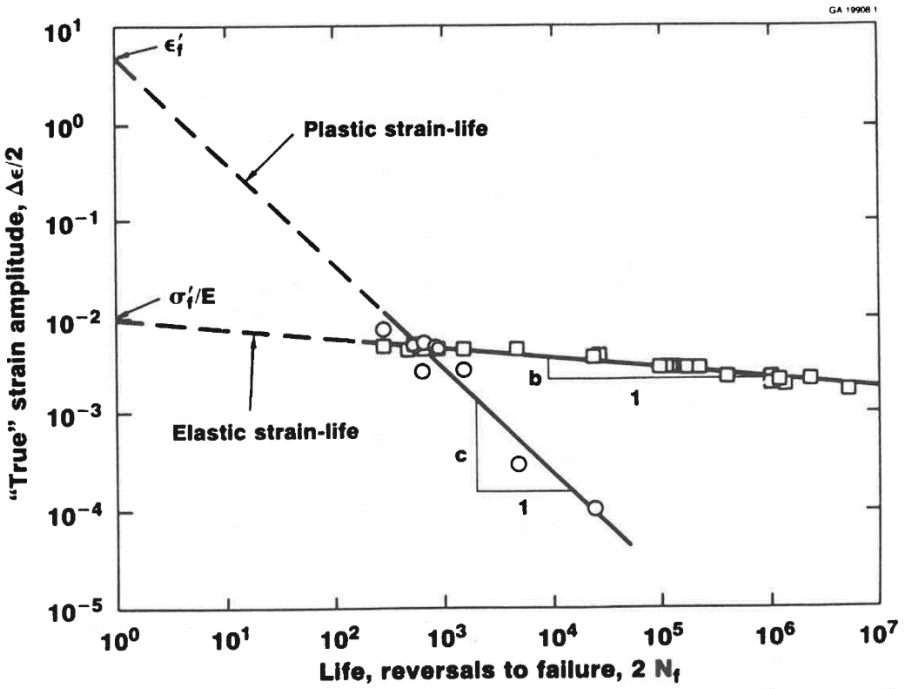

Figure 23 Strain-life plot of extruded AA6061-T6

Strain-life plot of extruded AA6061-T6 with elastic and plastic strain-life curves [21]

Table 3 Low-cycle fatigue properties for extruded AA6061-T6

Extruded AA6061-T6 LCF Parameters	**[3]**	**[4]**	**[5]**	**[16]**	**[21]**
Cyclic strain hardening exponent n'	0.025	0.078	0.044	0.039	0.024
Cyclic strength coefficient K' MPa	368.0	268.0	392.8	369.0	372.3
Fatigue strength coefficient σ_f' MPa	386.0	705.0	458.0	534.0	593.0
Fatigue strength exponent b	-0.036	-0.110	-0.063	-0.082	-0.093
Fatigue ductility coefficient ε_f'	0.770	2.400	0.620	4.490	5.390
Fatigue ductility exponent c	-1.010	-0.980	-0.750	-1.100	-1.100

Discussion of low-cycle fatigue data

One interesting finding from the LCF results presented by [3-5, 16] is the deformation induced hardening. Brammer et al. [4] and Mirza et al. [16] reported strain hardening between strain amplitudes of 0.2% to 0.6% and 0.6% to 1.2%, respectively. McCullough et al. [5] also reported strain hardening at 0.3%, however, the authors reported strain softening between strain amplitudes of 0.7% to 2.0%. In contrast, Badaruddin et al. [3] documented strain softening between amplitudes of 0.3% to 0.7% and strain hardening at amplitudes above 0.7%. Abood et al. [2] compared three different heat treatments on the strain-life of AA6061 in LCF. The three conditions were the O, T4, and T651 aged conditions. The LCF testing revealed that the O condition showed cyclic hardening while the other two conditions showed cyclic softening. Therefore, the strain hardening or softening behaviors were likely due to microstructural differences between each of the materials. Additionally, authors [3, 4, & 16] conducted the fatigue testing according to ASTM E606, while [5] performed testing according to ASTM E606-92 to achieve the higher strain amplitudes without buckling and [21] performed testing according to ASTM E606-80. Therefore, a difference in specimen sizes likely contributed to a difference in LCF response in addition to any microstructure variations.

All of the data analyzed in this study were collected from fully-reversed (R=-1) testing, however, it was noted that the strains were applied differently. The authors from [3] utilized a constant strain rate of 0.004 s^{-1} while [16 and 21] utilized a strain rate of 0.1 s^{-1}. The authors from [4 & 5] performed the cyclic testing at a constant frequency of 5 Hz instead of a constant strain rate. Therefore, the frequency of the fatigue testing for [3 & 16] changed continuously to hold the strain rate constant while the strain rate of the tests performed by [4 & 5] varied to keep the

frequency constant. The variation in rate of testing could have an effect on the outcome of the testing.

Tucker et al. [22] studied the plasticity, damage, and fracture characteristics of extruded AA6061-T6 at a variety of stress states and strain rates. Figure 24 shows the results from the from three strain rates in each of the stress states. Compression tests resulted in the highest stresses while tensile tests resulted in the lowest stresses, with torsion tests falling in between the two. At 6% equivalent strain, a 9% difference in flow stress was found between tension and compression results. Additionally, a 7% and 9% increase in tensile and compressive flow stress, respectively, was found between applied strain rates at 6% equivalent stain. Therefore, the stress state had an equal impact on flow stress as did the strain rate. Tension and torsional straining revealed higher damage nucleation rates than compression. It was also noted that compression loads showed the highest work hardening rate, while tension revealed the lowest work hardening rate.

The extruded AA6061-T6 incurred damage from micron-scale particles and nano-scale precipitates. Figure 25 is an optical microscope image of the AA6061-T6 with the extrusion direction perpendicular to the image. The Mg_2Si and AlFeSi secondary particles are indicated by the dark shapes. The secondary particles had an average diameter of 1.3 μm and an average nearest neighbor distance of 11.4 μm. The smaller precipitates (too small to be seen in Figure 25) were measured to have diameters ranging from 50-200 nm. Due to incurring void damage at two length scales, the void nucleation rate of the AA6061-T6 decreased as the strain rate increased. Additionally, the aspect ratio of the secondary particles was measured at 2.3.

Figure 26 shows scanning electron microscope images of the fracture surfaces of tensile specimens tested at a strain rate of .001/s and 1000/s. While both fracture surfaces show evidence of ductile fracture, the main difference is the size of the voids. As the strain rate increased, the

average size of the voids decreased. Therefore, due to a decrease in void nucleation rate and void size, the ductility increased as the strain rate increased. The alloy had an elongation to failure of 12.9% and 18.5% for the low and high strain rates, respectively. The percentage of small voids compared to the total number of voids increased from 39% to 98% for strain rates of 0.01/s and 1000/s, respectively.

Therefore, even though the stress state conditions for the data review from literature were all fully-reversed, it is likely that the differences in strain application from [3-5, 16, & 21] contributed to the differences in the LCF parameters.

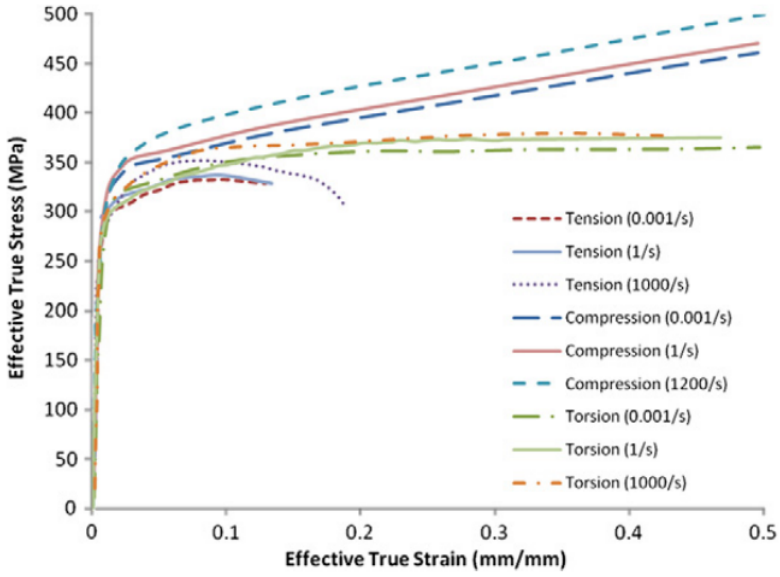

Figure 24 Effective stress-strain plot of extruded AA6061-T6

Effective stress-strain plot of extruded AA6061-T6 with varying stress states and strain rates [29]

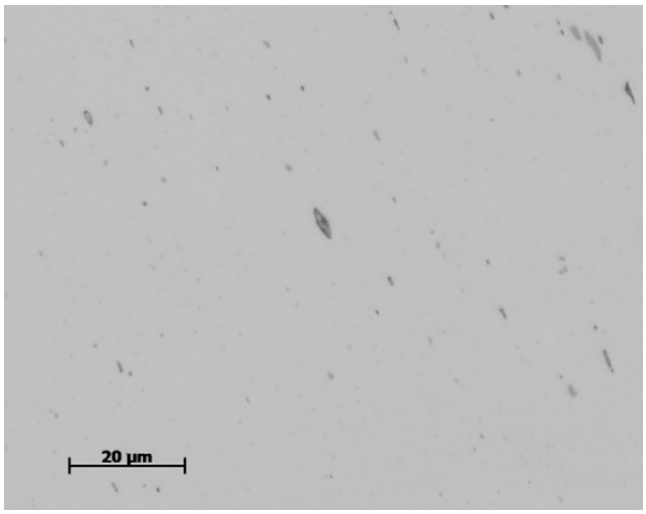

Figure 25 Optical microscopy image of extruded AA6061-T6 microstructure

Optical microscopy image of extruded AA6061-T6 revealing Mg2Si and AlFeSi secondary particles perpendicular to the extrusion direction [29]

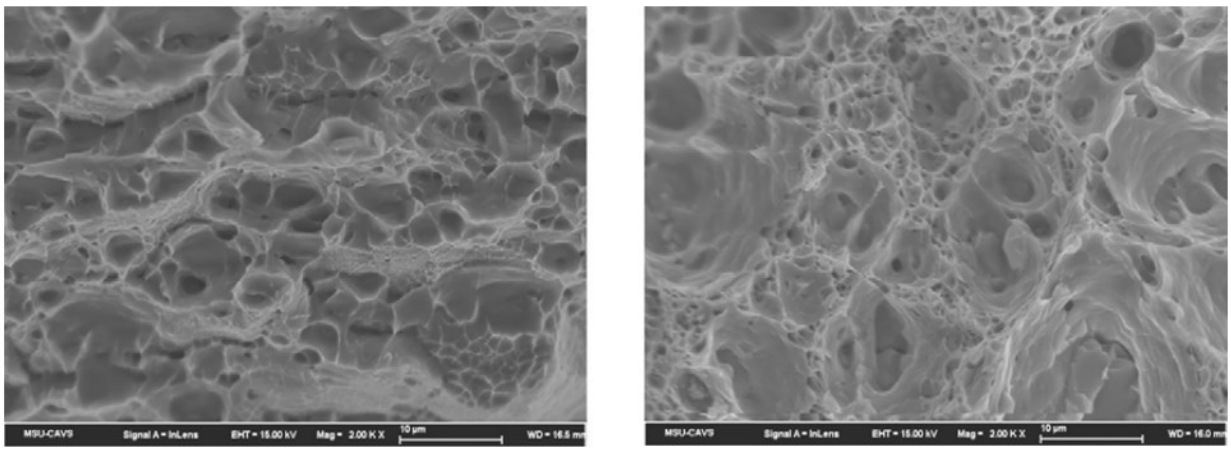

(a) (b)

Figure 26 Images pf extruded AA6061-T6 fracture surfaces

Images of extruded AA6061-T6 fracture surfaces under tension at strain rates of a) 0.0001/s and b) 1000/s [29]

Of utmost importance to this work was the low-cycle fatigue performance of extruded AA6061-T6. Several authors [3-5, 16, & 21] characterized the LCF parameters, which are summarized in Table 3. Additionally, McCullough et al. [5] quantified the LCF parameters for the MSF model, as shown in Table 4. The parameters defined in Table 3 do show some variation, however, none of the materials were tested exactly the same. Variations in strain amplitude, strain rate, and specimen size all had potential effects on the fatigue results. Even so, the cyclic strain hardening exponent n', the cyclic strength coefficient K', and the fatigue ductility exponent c showed consistency between [3, 16, and 21].

To summarize the literature review findings, the LCF properties of extruded AA6061-T6 have been evaluated and quantified by several sources. It was determined that the extrusion process results in a unique set of mechanical properties for AA6061-T6. Additionally, other factors affect the mechanical properties in addition to the processing history, such as material composition, heat treatment, and the application of the strain.

CHAPTER III

USER-DEFINED MATERIAL MODEL

For this work, a user defined material model (VUMAT) was employed within ABAQUS Explicit to accurately predict the response of the extruded AA6061-T6 during the finite element simulations. This material model featured Mississippi State University's plasticity-damage (DMG) and multi-stage fatigue (MSF) subroutines.

DMG plasticity-damage material model

To provide an accurate response from the finite element model, a viscoplasticity model created by Bammann et al. [23,24], known as the damage-plasticity, or DMG, model, was used in this approach to describe the nonlinear response of the extruded AA6061-T6 material behavior. The thermo-viscoplastic constitutive equations were developed from the classical thermodynamics of irreversible processes with internal state variables (ISVs). The evolution of the plasticity ISVs is prescribed in the hardening minus recovery format, where the hardening is defined as the increase in yield strength due to plastic deformation. The yield surface evolves in space in one of three ways for hardening materials: (1) isotropic hardening, k, which reflects the effect of the global dislocation density; (2) kinematic hardening, α, also known as the Baushinger effect, reflects the impact of the dislocation density; and (3) mixed hardening, where both isotropic and kinematic hardening characteristics are present. The orientation of the yield surface may change under mixed hardening. While the mixed hardening yield surface evolution has the greatest

potential accuracy of the three methods, isotropic hardening is the most commonly utilized method in finite element models for metal forming.

Overall, the mechanical properties of a material depend on the amount and type of defects within the microstructure. Deformation of a material increases the amount, size, and accumulation of these microstructural defects, increasing the amount of damage within the material. Microstructural damage reduces the material strength, increases the inelastic flow, and reduces the elastic moduli within the region of growth. The microstructural damage within ductile metals can typically be characterized through void nucleation, growth, and coalescence. If the extent of void growth prior to fracture is small, it is possible to ignore its effects on the constitutive equations, however, ductile fracture must include all three stages in order to provide a representative model.

Horstemeyer et al. [25] modified the DMG-plasticity damage model to account for stress state dependent damage evolution as well as the heterogeneities of microstructure for damage progression and failure analysis. The additions included grain size, particle size, particle volume fraction, pore size, pore volume fraction, and pore nearest neighbor distances. The pertinent equations within this model are denoted by the rate of change of the observable ISVs. The two components of the damage progression mechanism are void nucleation and second phase particle and pore growth. The time derivative of damage total ϕ_{total} is shown in Equation 7.

$$\phi_{total} = \left(\dot{\phi}_{particles} + \dot{\phi}_{pores}\right)C + \left(\phi_{particles} + \phi_{pores}\right)\dot{C} \tag{7}$$

Where the damage variable ϕ_{total} represents the damage fraction of material within a continuum element. The parameters $\phi_{particles}$ and ϕ_{pores} represent the void growth from the particle debonding and from pores, respectively, while $\dot{\phi}_{particles}$ and $\dot{\phi}_{particles}$ are their respective time

derivatives. The variable C represents the void coalescence, which is indicative of the pore-pore and particle-pore interactions, and $\dot{C}$ is its time derivative. Failure is assumed to have occurred when the damage fraction approaches unity.

The DMG plasticity-damage material model was implemented into a finite element subroutine for solving the plasticity and damage equations simultaneously due to the coupling of the damage and stress equations. Within this framework, all of the ISV model accounts for the deviatoric inelastic deformation resulting from the presence of dislocations, dilatational deformation, and the ensuing failure from damage progression. Therefore, the ISV equations work together to link the microstructural features to the macroscopic response of the material. Failure state is reached within an element as ϕ_{total} approaches a value of 1.

A total of 58 parameters were used to characterize the extruded AA6061-T6 within the subroutine for the DMG model, which can be seen in Table 4. The DMG parameters were provided by Mississippi State University.

Table 4 Damage-plasticity model parameters used in the VUMAT

Coefficient	Modified Extruded AA6061-T6 Values
θ_0	293
ρ	2.7E-09
Cv	0.372024
E	66380
v	0.33
$C01$	3.15717
$C02$	0
$C03$	276
$C04$	0
$C05$	.0005
$C06$	0
$C07$	0.692991
$C08$	0
$C09$	739.464
$C10$	0
$C11$	0
$C12$	0
$C13$	0.985029
$C14$	0
$C15$	539.246
$C16$	0
$C17$	0
$C18$	0
$C19$	0.011853

Table 4 (continued)

Coefficient	Modified Extruded AA6061-T6 Values
$C20$	567.441
$C21$	0
Ca	0
Cb	0
DC	0.99
an	0
bn	0
cn	0
$Ccoef$	0
$XKIC$	1000
ASP	0
PVF	0.001
$cd1$	1
$cd2$	1
$dcs0$	30
dcs	30
ZZ	0.509
$VVFI$	0
CTN	0
CTC	0
DN	0.01
$r0$	0
$BETAE$	1
CAM	18

Table 4 (continued)

Coefficient	Modified Extruded AA6061-T6 Values
$EPSF$	1.0e-10
$VNEWDT$	0.50
$NPLAS$	1
NCD	10
$NVOL$	0
$NPLAN$	0
$NLGEOM$	0
NT	0
$NITMAX$	0.25
M	0

Multi-stage fatigue model

The multi-stage fatigue (MSF) model was introduced by [26-28] and has since been expanded upon by [5, 29-32] to capture predictable fatigue behavior for a variety of aluminum alloys in both low- and high-cycle fatigue with respect to their processing histories. The MSF model was originally developed to capture the high-cycle fatigue of cast Al-Mg-Si alloys by identifying the effect of various microstructural features, such as pores, inclusions, etc. More specifically, the MSF model characterizes the effect of constrained microplasticity at debonded particles or pores on the formation and growth of microstructurally-small fatigue cracks. The MSF model focuses on the cyclic crack displacement as the driving force for crack growth instead of the traditional linear elastic fracture mechanics approach featuring the range of stress intensity, ΔK. The MSF model

incorporates the incubation (INC), microstructurally small crack (MSC), physically small crack (PSC), and long crack (LC) stages of fatigue to predict the fatigue behavior of specific metals undergoing particular material processing methods, as related in Equation 8,

$$N_{total} = N_{INC} + N_{MSC/PSC} + N_{LC} \quad (8)$$

where, N_{total} is the total fatigue life in number of cycles. N_{INC} is the number of cycles required to incubate a crack at a microscopic notch. The crack is considered incubated once the crack length reaches approximately one-half of the diameter of the void or inclusion that generates the crack. $N_{MSC/PSC}$ is the number of combined cycles required to propagate a MSC and a PSC from the microscopic notch. The MSC is defined as a crack with a length ranging between one-half the inclusion diameter up to 3 times the smallest grain size within the microstructure. The crack is considered a PSC when the size ranges from 3 times the smallest grain size up to 0.3 mm or even 3.0 mm depending on the microstructure. N_{LC} is the number of cycles required for the LC to propagate until fracture. The LC would be considered any crack larger than the PLC, therefore, it could be as small as 0.3 mm.

Incubation

To capture the INC phase of the fatigue life of a material, the MSF utilizes a modified Coffin-Manson law based on the non-local maximum plastic shear strain, which is optimized for microscale interactions, as shown in Equation 9. In Equation 9, C_{inc} represents the linear coefficient while α represents the exponential coefficient within the modified Coffin-Manson law. The damage around the incubation site is characterized by the parameter β, which is the non-local

maximum plastic shear strain amplitude over an area that is approximately one percent of the total inclusion area. The expression $\frac{\Delta\gamma_{max}^{p*}}{2}$ represents the local average amplitude of the maximum plastic shear strain, while ε_a is the remote applied strain amplitude and ε_{th} represents the micro-plasticity strain threshold. The variable ψ integrates measured microstructural properties into the incubation parameter to increase the model sensitivity to variance within the microstructure. The parameter ψ can be defined by the expression $\psi = \left[\frac{(MPS)^2}{(NND)(GS)}\right]^{\lambda}$, which utilizes the maximum particle size (MPS), the nearest neighbor distance (NND), the grain size (GS), and a sensitivity exponent (λ). The coefficient C_{inc} can also be defined by Equation 10, where c_n is a material dependent constant and the parameter R is the load ratio based on the maximal principal stress.

$$C_{inc}N_{inc}^{\alpha} = \frac{\Delta\gamma_{max}^{p*}}{2} = \beta = \psi\bar{Y}[\varepsilon_a - \varepsilon_{th}]^q \tag{9}$$

$$C_{inc} = c_n(1 - R) \tag{10}$$

Equation 11 accounts for the relationship between the local plastic shear strain and the remote applied strain. The variables y_1 and y_2 are constants related to the remote applied strain translation of the local plastic shear strain. When the length of the plastic zone in front of the inclusion reaches its saturated length (η_{lim}), which can be described as the transition between constrained microplasticity and unconstrained microplasticity [33], Equation 12 is generated for the parameter $\bar{Y}$; where $\frac{l}{D}$ is the nominal length of the plasticity zone divided by the diameter of the inclusion or void where the crack is incubating.

$$Y = y_1 + (1 + R) * y_2 \tag{11}$$

$$\bar{Y} = \left(1 + \zeta * \frac{l}{D}\right) Y \tag{12}$$

When $\frac{l}{D}$ is less than or equal to η_{lim}, the ratio is defined by Equation 13. When $\frac{l}{D}$ is greater than η_{lim}, it can be defined by Equation 14. In Equation 14, r is the shape constant for the limited plasticity transition [34-35]. The percolation limit, ε_{per}, and the strain threshold, ε_{th}, were determined through micro-mechanical simulations.

$$\frac{l}{D} = \eta_{lim} \frac{\varepsilon_a - \varepsilon_{th}}{\varepsilon_{per} - \varepsilon_{th}}, \qquad \frac{l}{D} \leq \eta_{lim} \tag{13}$$

$$\frac{l}{D} = 1 - (1 - \eta_{lim}) \left(\frac{\varepsilon_{per}}{\varepsilon_a}\right)^r, \qquad \eta_{lim} < \frac{l}{D} \leq 1 \tag{14}$$

It has also been shown in literature [29] that the two strain values can be quantified through standard endurance limit calculations, as shown in Equations 15 and 16; where S_{ut} is equal to the ultimate tensile strength, σ_y^{cyclic} is equal to the stabilized cyclic yield strength, and E is the elastic modulus.

$$\varepsilon_{th} = \frac{0.29 S_{ut}}{E} \tag{15}$$

$$I\varepsilon_{per} = \frac{0.7 \sigma_y^{cyclic}}{E} \tag{16}$$

Small crack

When the localized plastic zone has reached saturation, the crack transitions from the incubation phase into the MSC and PSC regime. The MSC/PSC crack growth within the MSF is captured through the range of the crack tip displacement, or ΔCTD. In high cycle fatigue, the ΔCTD would be related to the crack length and the applied stress amplitude, however, in low-cycle fatigue, ΔCTD is proportional to the macroscopic shear strain range. Equation 17 defines the crack growth rate with respect to the number of cycles as a function of ΔCTD; where χ is a material constant related to the crack propagation rate within the microstructure in which the crack growth rate is linearly proportional to the crack driving force [25]. ΔCTD_{th} is the threshold value for the crack tip displacement, which is $2.85*10^{-4}$ μm for pure FCC aluminum. The parameter a_i represents the initial crack length with respect to the inclusion size.

$$\left(\frac{da}{dN}\right)_{MSC} = \chi(\Delta CTD - \Delta \mathrm{CTD}_{th}), a_i = 0.625D \tag{17}$$

Equation 18 represents the crack tip displacement as a function of the remote loading application; where C_I, C_{II}, ω, and ζ are material dependent parameters that capture the microstructure-specific effects of the MSC growth in both low-cycle and high-cycle fatigue. The expression $\left(\frac{GS}{GS_0}\right)^{\omega}$ accounts for the effect of grain size on small crack growth, where GS is the grain size under consideration, GS_0 is the reference grain size [29].

$$\Delta CTD = C_{II}\psi\left(\frac{GS}{GS_0}\right)^{\omega}\left[\frac{U\Delta\hat{\sigma}}{S_{ut}}\right]^{\zeta} a_i + C_I\psi\left(\frac{GS}{GS_0}\right)^{\omega}\left(\frac{\Delta\gamma^p_{max}}{2}\right)^2 \tag{18}$$

The parameter $\Delta\hat{\sigma}$ is defined by Equation 19; where $\Delta\bar{\sigma}_a$ is equal to the uniaxial effective stress amplitude $\left(\sqrt{\frac{3}{2}\frac{\Delta\sigma'_{ij}}{2}\frac{\Delta\sigma'_{ij}}{2}}\right)$, $\Delta\sigma_1$ equals the maximum principal stress range and θ is equal to the path dependent loading parameter [36], where $0 \leq \theta \leq 1$. The parameter U accounts for the effect of the loading ratio, where $U = \frac{1}{1-R}$.

$$\Delta\hat{\sigma} = 2\theta\bar{\sigma}_a + (1-\theta)\Delta\sigma_1 \tag{19}$$

Long crack

The MSF model holds the ability to either account for damage from long crack growth through linear elastic fracture mechanics (LEFM) or it can be coupled with a more complex fracture mechanics model such as Fastran [37]. The LEFM approach focuses on the range of the stress intensity factor, ΔK. Paris et al. [38] developed Equation 20, which shows a linear relationship between the crack growth rate and the stress intensity factor on a log-log scale,

$$\frac{da}{dN} = A(\Delta K)^n \tag{20}$$

where, A is the crack growth parameter and n is the exponent in the Paris Law. Considering the failure mechanisms of a ductile metal such as aluminum, the long crack contribution to fatigue life in terms of cycles is relatively limited because it typically occurs at the millimeter length scale [24], therefore the INC and MSC/PSC stages represent the majority of the fatigue life of similar metals [32, 39-40].

A total of 43 parameters were used within the MSF model to decompose the damage progression into the four stages of crack growth for the extruded AA6061-T6, as shown in Table 5. Maximum cycle limits of 5,000, 1,500, and 15 cycles were applied for the INC, MSC/PSC, and LC stages, respectively, to reduce the computation time.

The main goal of this work is to characterize the LCF performance of the extruded AA6061-T6 AM2 matting connection via a 3D FEM in conjunction with the DMG-MSF user-defined material model.

Table 5 Multi-stage fatigue model parameters

Stage	Coefficient	Extruded AA6061-T6 [5]	Modified Extruded AA6061-T6
		Values	Values
INC	K'	392.9	392.9
	n'	0.0438	0.0438
	C_{inc}	0.60	0.60
	C_m	0.6228	0.6228
	A	-0.74	-0.74
	Q	2.27	2.27
	y_1	365.2	365.2
	y_2	1,422	1,422
	ζ	1	1
	R	2.78	2.78
	E_{MODEX}	1	1
	$PART_{EXP}$	1	1
	Ω	0.50	0.50
MSC/PSC	a_i	0.25	0.25
	Θ	1.0	1.0
	Z	1.35	1.35
	CI	16,000	16,000
	CII	0.07	0.07
	χ	0.425	0.425
	CTD_{TH}	0.000285	0.000285
	a_{final}	450	450
	DCS_{EXP}	1	1
	$PORE_{EXP}$	0	0
	$GO - EXP$	0	0

Table 5 (continued)

Stage	Coefficient	Extruded AA6061-T6 [5] Values	Modified Extruded AA6061-T6 Values
	PM	0.324	3.76
	$YGCF$	0.140	1
	Gs	12.3	12.3
	$G0$	2.07	2.07

Multi-stage fatigue model parameters for extruded AA6061-T6 from [5] and the modified parameters used for this study

CHAPTER IV

EXPERIMENT

The purpose of this work is to build a finite element model to characterize the fatigue behavior of the extruded AA6061-T6 AM2 matting locking connection over a 6 CBR subgrade using the DMG-MSF material models.

Finite element analysis

A 3-D finite element model of the extruded AA6061-T6 AM2 locking connection was analyzed using ABAQUS Explicit. A two-inch wide section of the joint was modeled for simplicity and also to best represent the laboratory testing performed previously by [7,8]. For this work, the overlapping and underlapping end connectors have the same 5.08 cm (2.0 in.) width and 3.81 cm (1.5 in.) height, however, for simplicity, each rectangular hollow core and end connector were modeled as one piece instead of accounting for the welded region and insert. Additionally, the weld is not an area of interest for this work since the locking tabs, or teeth, typically fail before the welded region. The rollers on the right hand side and the upper roller on the left hand side from Figure 3 were assembled in the same location as [7,8] as shown in Figure 27. The lower roller on the left hand side was adjusted from 21 cm to 27 cm from the center of the joint to account for the increased stiffness in the FEM. The model boundary conditions were verified by using the same calibration procedure as [7], which resulted in the same displacement of 1.59 cm (0.625 in.) at the center of the loading roller when a 13.3 kN (3,000 lbf) load was applied, as shown in Figure 28.

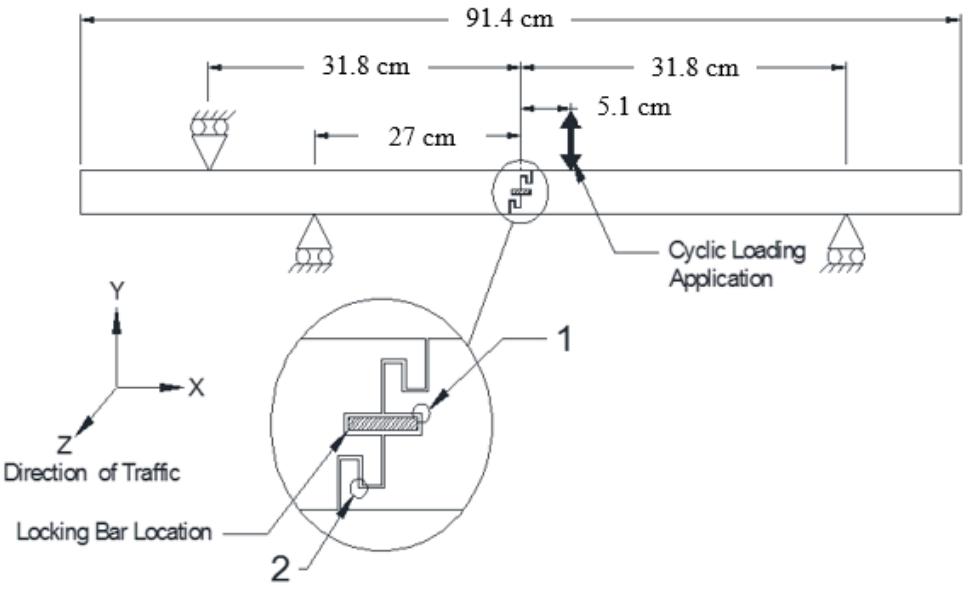

Figure 27 Schematic of boundary conditions used for the 3D FEM

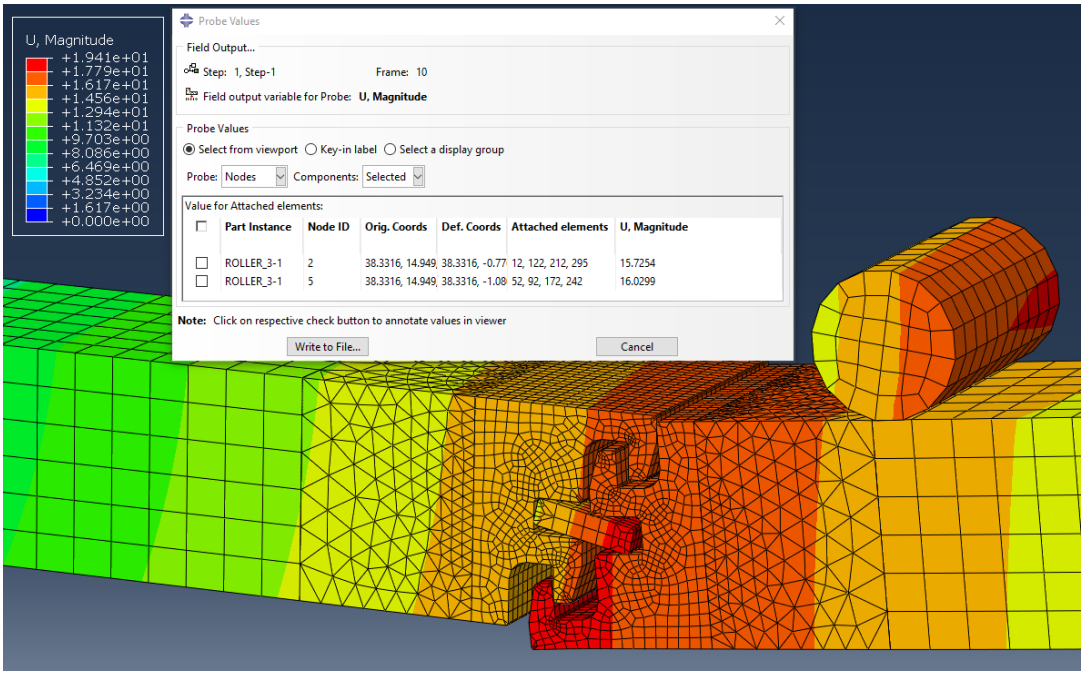

Figure 28 Snapshot of 3D FEM after an applied calibration load of 13.3 kN

Figure 29 depicts the setup of the FEM. Boundary conditions of a roller (zero displacement in the U1-, U2-, U3-, UR1-, and UR2-directions) were applied to both rollers on the left hand side as well as the lower roller on the right hand side of the model. The upper roller on the right hand, or underlap, side of the connection had a zero displacement boundary condition for the U1-, U3-, UR1-, and UR2-directions and a specified displacement of -21.23 mm was applied in the negative U2-direction. All of the boundary conditions were applied during a single step with a time period of 1.0 and mass scaling at a factor of 1,000. The boundary conditions were applied with a smooth amplitude where the output is 0 at time 0 and 1 at time 1. The controlling displacement is plotted versus the step time in Figure 30. The specific geometry of the connection was provided by the U.S. Army ERDC and cannot be presented here to protect the IP.

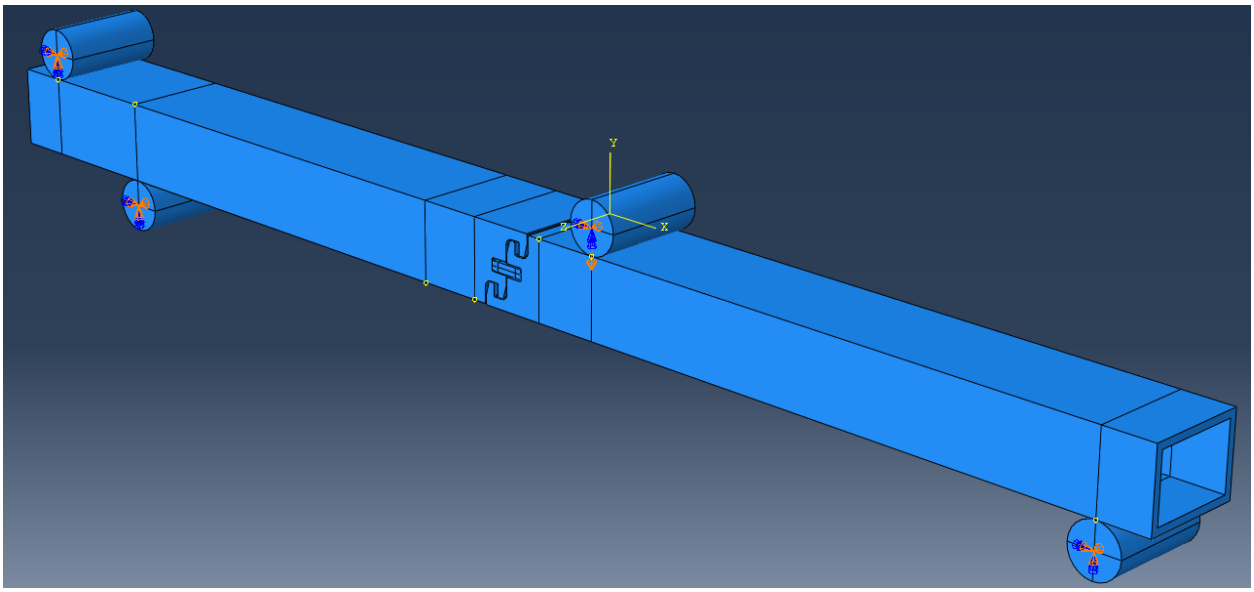

Figure 29 Picture of the boundary conditions applied to the FEM

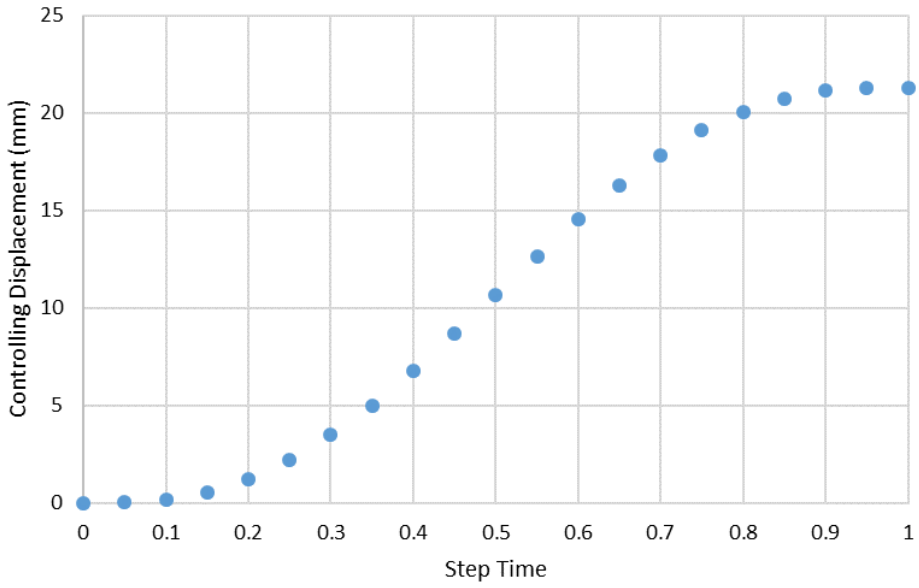

Figure 30 Graphical plot of the controlling amplitude versus the step time for the FEM

General contact was applied (all with self) to the whole model. Tangential behavior contact properties were applied with a friction penalty of 0.1 to provide a small amount of friction to the surfaces as they interact with each other.

Linear C3D8R hexahedron elements were used for most of the model, however, a transition region between the course and fine elements utilized C3D10M quadratic tetrahedron elements, as shown in Figure 31. The element size was decreased in the area of interest (shown in Figure 32) to avoid singularities and for better convergence across areas of high stress and strain gradients. The maximum aspect ratio of elements within the area of interest was measured at 6.75 for the coarsest mesh.

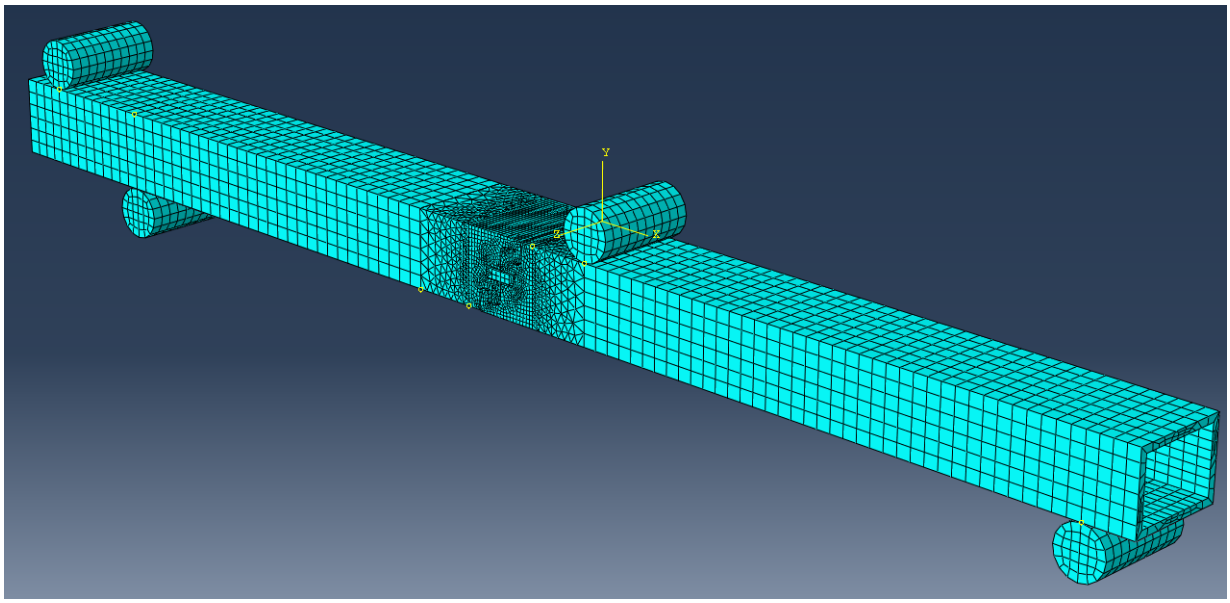

Figure 31 Snapshot of the meshes applied to each component of the FEM

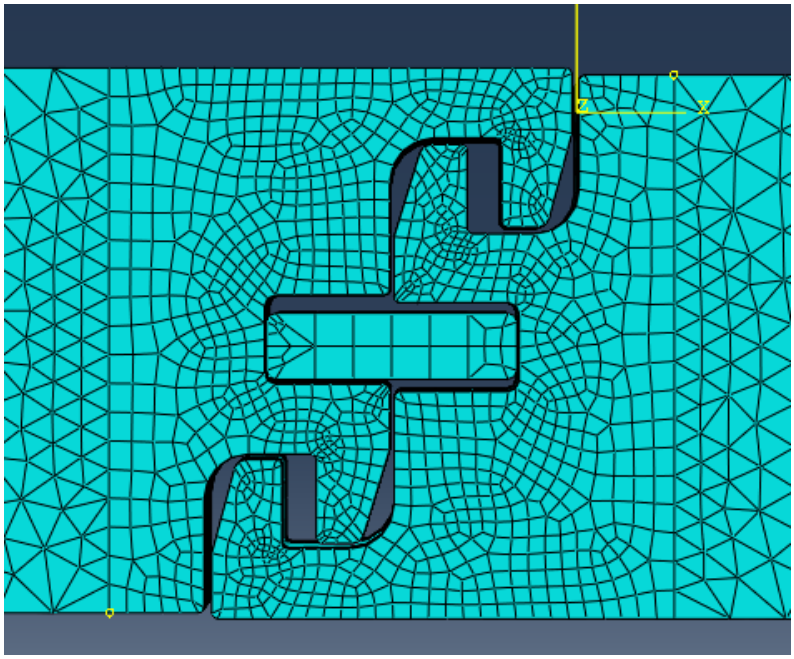

Figure 32 Close-up view of the meshed area of interest

Three different material properties were applied to the model. Purely-elastic 17-4 PH stainless steel properties were applied to the rollers since they were not the focus of this study. A Young's modulus of 1.9E05 GPa, a Poisson's ratio of 0.27, and a density of 7.75E-09 tonne/mm^3 were utilized. The properties are summarized in Table 6. Additionally, purely-elastic, purely-plastic AA6061-T6 properties were utilized for the material within the connectors that was outside of the area of interest. A Young's modulus of 66,380 GPa, a Poisson's ratio of 0.33, a yield stress of 304.4 MPa, and a density of 2.9E-09 tonne/mm^3 were applied. These material properties are also summarized in Table 6. For the material within the area of interest, 101 parameters were used to characterize the extruded AA6061-T6 for the DMG and MSF models. The MSF model parameters were calibrated with the as-received extruded AA6061-T6 data from [5]. The DMG model utilizes 58 material specific parameters while the remaining 43 parameters were calibrated through the MSF model with the as-received material data from [5]. The data from [5] were recorded from fully-reversed strain life fatigue testing at a frequency of 1 Hz for strain amplitudes above 0.7% and a frequency of 5 Hz at 0.7% and below. The 101 total parameters for the extruded AA6061-T6 were applied to the FEM through a user-defined material model, or VUMAT, subroutine.

Table 6 Table of material properties used outside of the area of interest

Property	17-4 PH SS	AA6061-T6
EMOD (Gpa)	1.90E+05	6.64E+04
Poisson's Ratio	2.70E-01	3.30E-01
Density (tonne/mm3)	7.75E-09	2.70E-09
Yield Strength (Mpa)	--	3.04E+02

To ensure the calibration of the DMG-MSFVUMAT, a single element finite element analysis was performed. A single C3D8R element was meshed, as shown in Figure 33, with all dimensions measuring 25.4 mm. X-Symmetry was applied to the base, or XZ plane, of the element while the right and rear (XY and YZ) surfaces of the element were restricted to Z-Symmetry and X-Symmetry, respectively. A displacement of 1 mm was applied to the front surface of the element in the U1-direction to achieve a desired strain amplitude within the element. All of the boundary conditions were applied through a single step and utilized a smooth amplitude where the output is 0 at time 0 and the output is 1 at time 1. Figure 34 displays the strain-life results for the DMG-MSF subroutine in conjunction with the single element model and compares it to the strain-life fatigue data from [5]. The DMG-MSFVUMAT correlates well with the fatigue data provide by [5], showing that the material properties are well calibrated and are applied correctly to the FEM. Mass scaling was also applied to the model with a factor of 1,000 to decrease computation time. The parameters PM and $YGCF$ were modified from 0.324 and 0.140 to 3.76 and 1, respectively, during the single element FEM calibration of the material model to allow the model to run properly. The parameter PM is the Paris exponent and the parameter $YGCF$ is the geometrical correction function. Both constants are long crack parameter, therefore, they should have a minimal effect in the LCF regime.

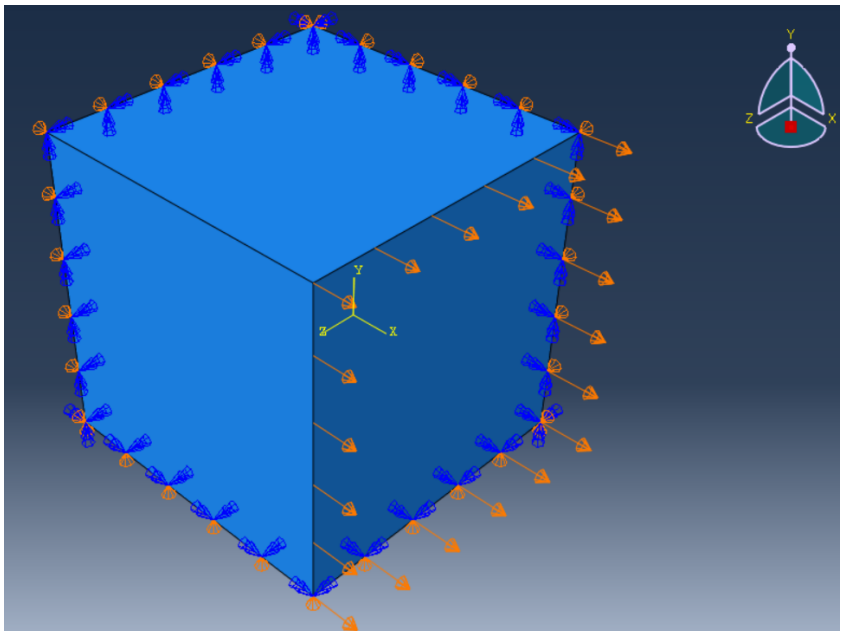

Figure 33 Image of the single element FEM boundary conditions for the DMG-MSF calibration

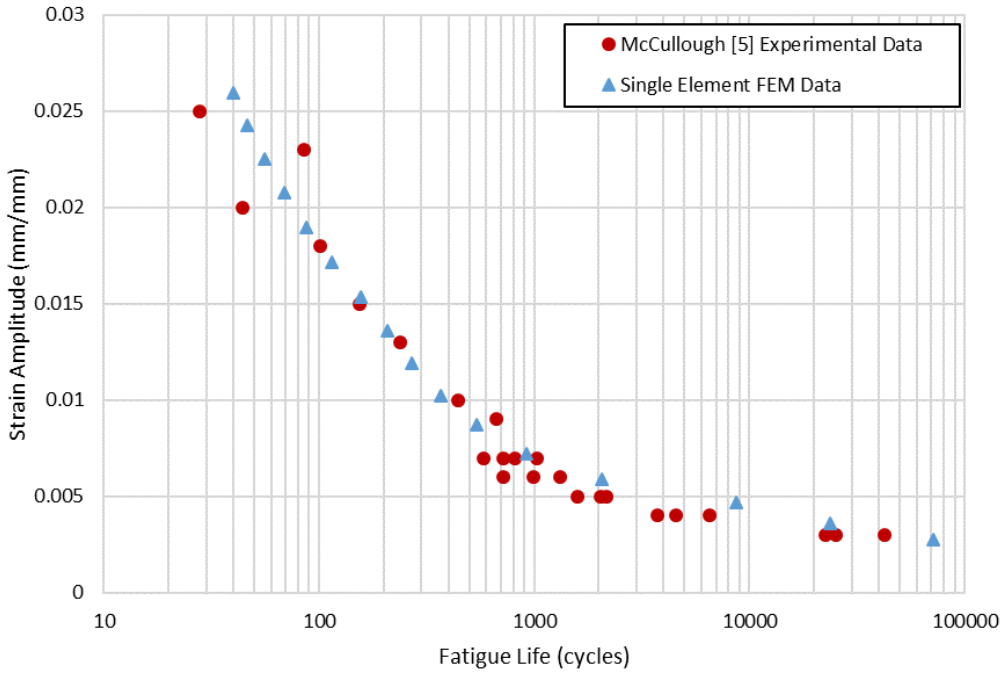

Figure 34 Strain-life plot of the single element FEM results compared to laboratory data

Laboratory data provided by [5]

Results

Figure 35 shows the finite element model of the AM2 connection at the maximum displacement of 21.32 mm in the negative U2 direction, which is equal to the rut depth or actuator displacement at cycle 1,132. The results provided herein are reported from the underlapping connector of the system. The maximum Von Mises stress was found to be 341.1 MPa and was located within the lower tooth. The upper tooth of the underlapping joint revealed very similar Von Mises stresses as the lower tooth, but slightly lower at 313 MPa. As expected, the maximum principal logarithmic strain value of 7.8E-02 mm/mm was also located in the same location as the maximum stress, as seen in Figure 36a. The maximum principal logarithmic strain in the upper tooth of the connector was approximately 2.9E-02 mm/mm. The maximum effective strain amplitude (SDV 53) was found to be 4.4E-02 mm/mm, as shown in Figure 36b, while the effective strain amplitude within the upper tooth was recorded at 1.5E-02 mm/mm.

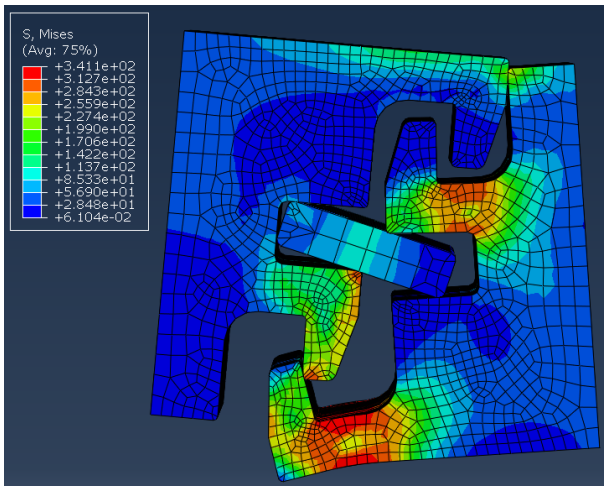

Figure 35 Contour plot of the Von Mises stress at a displacement of 21.32 mm

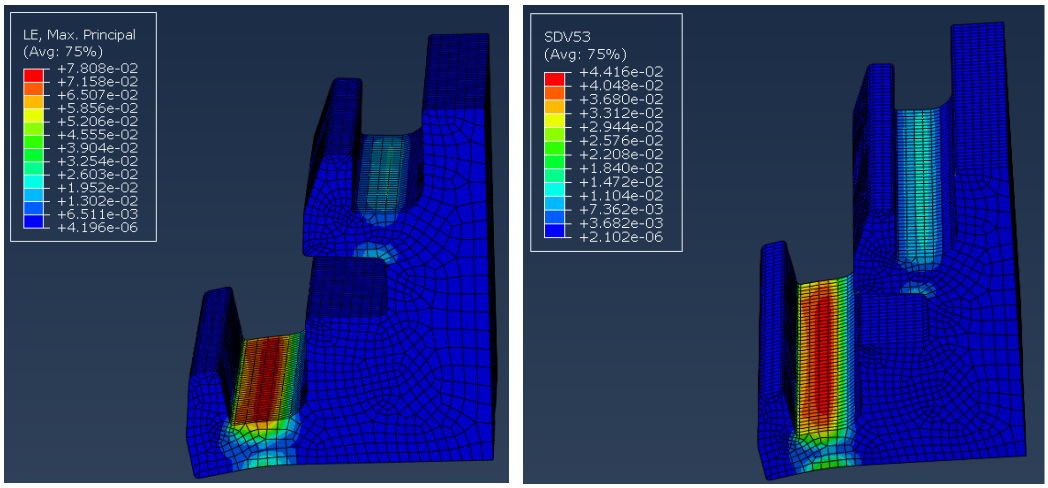

Figure 36 Principal and effective strain contour plots of the underlapping connector

Showing a) the principal logarithmic strain and b) the effective strain amplitude within the underlapping connector at a displacement of 21.32 mm

The predicted fatigue life (SDV 61) was approximately 11 cycles for the lower tooth and 158 cycles for the upper tooth, which can be seen in Figure 37. The total fatigue life can be broken down into its respective components of INC, MSC/PSC, and LC to better understand the failure. Figure 38a shows the total incubation period (SDV 58) within the underlapping connector. The number of INC cycles predicted in the lower tooth was approximately 4 cycles. The number of INC cycles in the upper tooth was approximately 129. Figure 38b displays the MSC/PSC (SDV 59) results for the underlapping connector. The DMG-MSF model predicted 7 total MSC/PSC cycles for the lower tooth and 29 cycles for upper tooth. The LC stage (SDV 60) reported zero cycles for the stressed areas of both the upper and lower tooth of the underlapping connector.

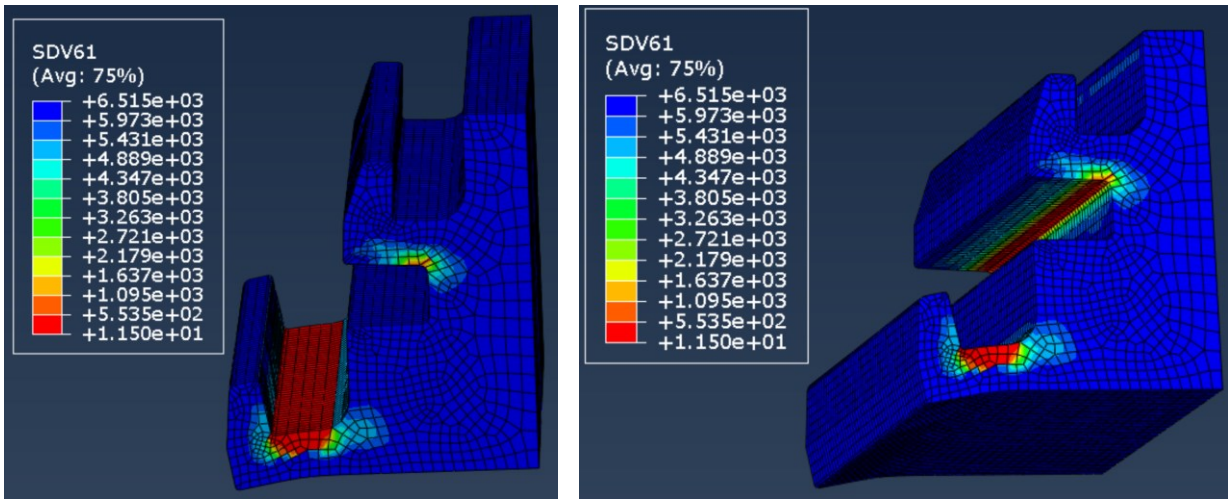

Figure 37 Contour plots of the predicted fatigue life for the underlapping connector from two different angles at the maximum displacement of 21.32 mm

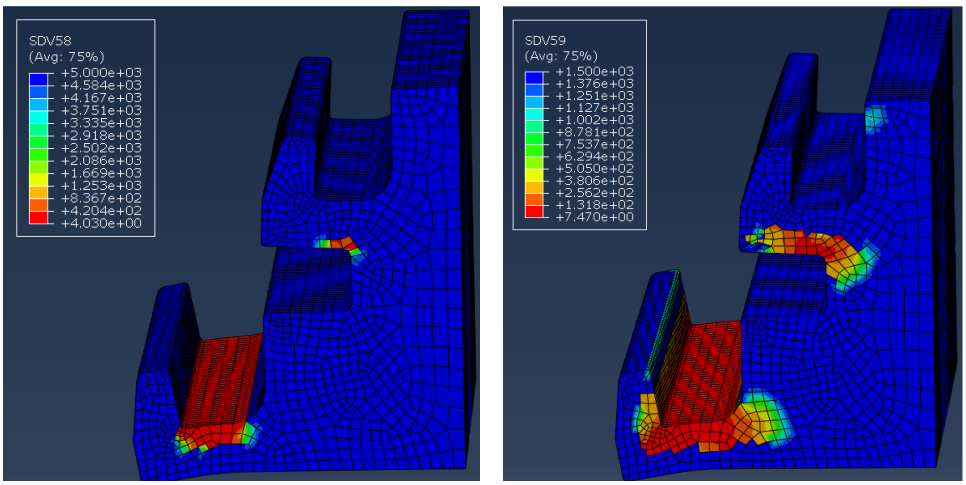

(a) (b)

Figure 38 Contour plots of the underlapping connector for the INC and MSC/PSC stages

Section a) depicts the INC (SDV 58) regime and b) depicts the MSC/PSC regime of the total fatigue lives in the underlapping connector at a displacement of 21.32 mm

A mesh convergence study performed on the FEM to ensure the convergence of the results. Figure 39 shows a plot of the maximum effective strain amplitude versus the number of elements at within the lower tooth of the underlapping connector. The h-refinement method was used for the area of interest by increasing the number of elements in the area of large stress and strain gradients. The total number of elements meshed within the two connectors ranged from approximately 5.0E04 to 1.0E05 and the element density was only changed in the area of interest. The highest aspect ratio within the underlapping connector ranged from 6.8 to 3.8 for the least- and most-dense meshes, respectively. The maximum Von Mises stress, principal logarithmic strain, effective strain amplitude, and predicted fatigue life was recorded for each simulation within the convergence study, as shown in Table 7.

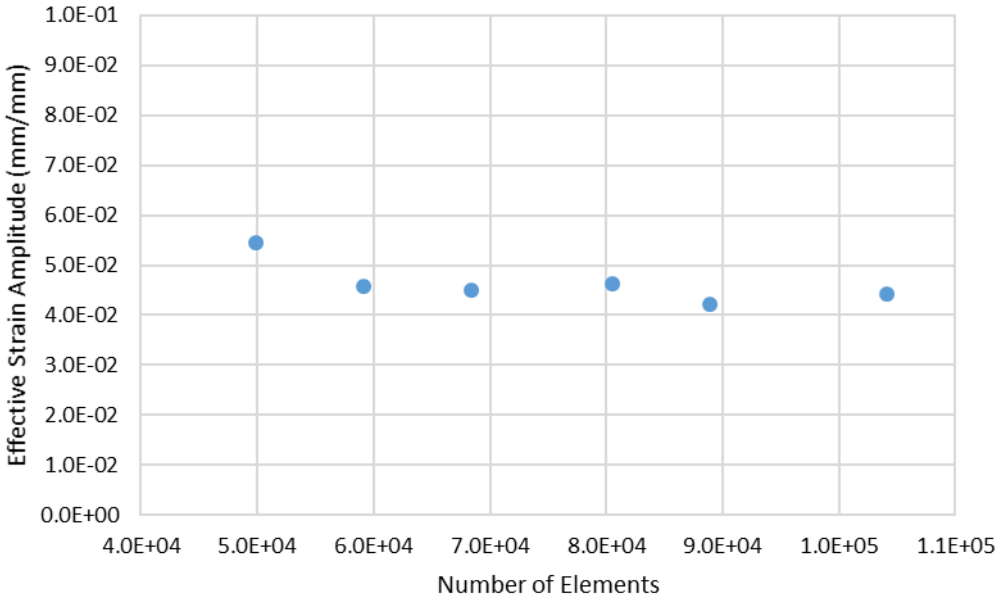

Figure 39 A plot of the effective strain amplitude versus the number of elements for the mesh convergence study of the FEM

Table 7 Tabulated results from the mesh convergence study performed on the FEM

Total Elements	Max Aspect Ratio	Max Von Mises Stress (MPa)	Max Principal Logarithmic Strain (mm/mm)	Max Effective Strain Amp (mm/mm)
4.98E+04	6.8	340.5	9.72E-02	5.45E-02
5.91E+04	5.8	341.2	8.08E-02	4.57E-02
6.84E+04	5.0	340.7	8.04E-02	4.51E-02
8.05E+04	4.6	339.8	8.26E-02	4.64E-02
8.89E+04	4.2	339.9	7.45E-02	4.21E-02
1.04E+05	3.8	341.1	7.81E-02	4.42E-02

Discussion

It is interesting to note that out of the 11 total cycles the MSF-DMG model predicted for the lower tooth, 4 cycles were in the INC stage and then the remaining 7 cycles were within the MSC/PSC stage of crack propagation. In contrast, the upper tooth predicted a total fatigue life of 158 cycles, however, 129 of the cycles were in incubation and only 29 were propagation of the MSC/PSC. An increase from the effective strain amplitude of 1.5E-02 mm/mm in the upper tooth to the effective strain amplitude of 4.4E-02 mm/mm in the lower tooth caused a decrease in the INC cycles from 128 to 4. The MSC/PSC stage only reduced from 29 to 7 cycles. Therefore, the incubation period is the controlling stage of the fatigue life in LCF.

For this work, the upper tooth of the underlapping connector was the main area of interest because it is the most common failure location observed by [6-9]. The maximum stress and strain values within the connection are reported on the lower tooth of the underlapping connector, however, the lower tooth is not the typical failure point. It is interesting to note that the upper tooth reported higher strain values than the lower tooth from step time 0.0 to step time 0.65, which is

equal to joint displacements of 0.0 mm and 16.31 mm, respectively, which is almost 77% of the maximum vertical travel. Figure 40 is a snapshot of the effective strain amplitude contour plot of the underlapping connector at step time 0.65. The maximum values of the contour plot were limited to reduce the effect of the singularities caused by the contact of the locking bar. The recorded effective strain amplitude within the upper tooth at step time 0.65 was approximately 8.9E-3 mm/mm, which corresponded to a predicted fatigue life of about 520 cycles.

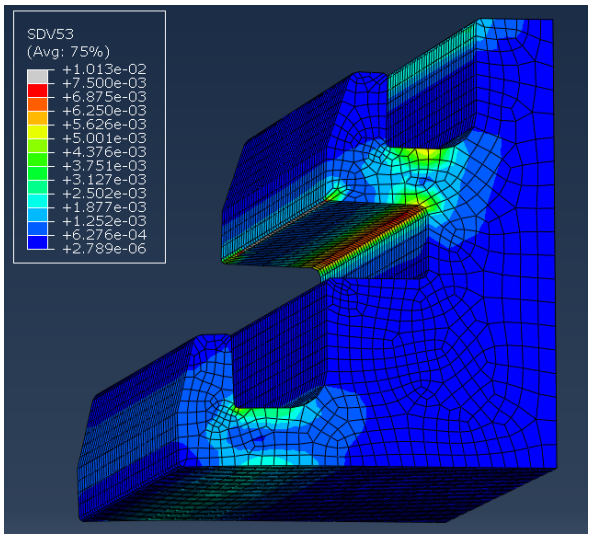

Figure 40 Contour plot of the effective strain amplitude within the underlapping connector at step time 0.65

According to Figure 34, the FEM needed to calculate an effective strain amplitude of 6.5E-03 mm/mm in order to get the same fatigue life as the laboratory- and full-scale testing. The FEM calculated the effective strain amplitude to be 6.5E-03 mm/mm in the upper tooth between step times 0.60 and 0.65, which are equal to 14.55 mm and 16.31 mm of vertical travel, respectively. The effective strain amplitude in the upper tooth measured approximately 5.2E-03 mm/mm and 8.9E-03 mm/mm for steps 0.60 and 0.65, respectively. Interpolating Figure 30 between steps 0.60

and 0.65 provided an equivalent constant amplitude displacement of 15.17 mm in order to provide the same fatigue life as the existing data, which is 71% of the total displacement.

The FEM was re-submitted with a maximum displacement of 15.17 mm and the results are shown below. Figure 41 shows a contour plot of the Von Mises stresses and Figure 42 shows the logarithmic strains found within the underlapping and overlapping sides of the connection. A maximum stress of 292.4 MPa and logarithmic strain of 1.45E-02 was recorded within the upper tooth of the underlapping connector and the maximum effective strain amplitude in the upper tooth was approximately 6.8E-03, as shown in Figure 43.

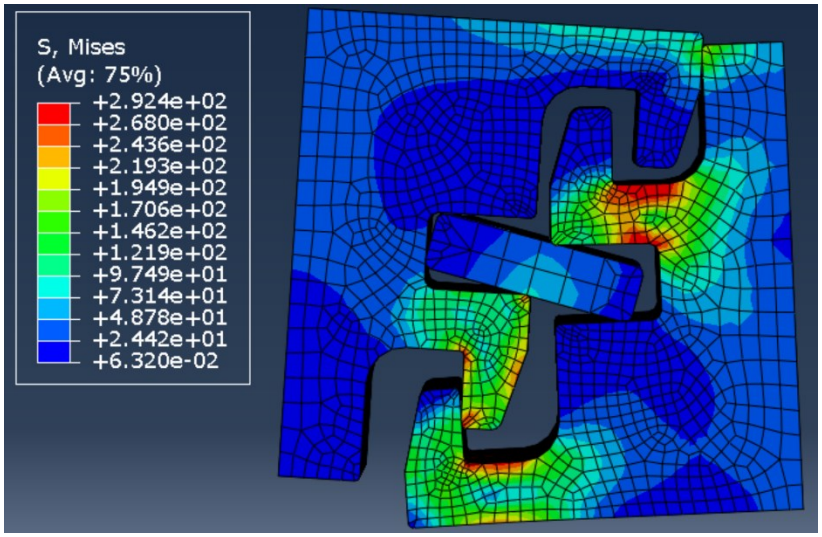

Figure 41 A contour plot of the Von Mises stress within the connection system at a displacement of 15.17 mm

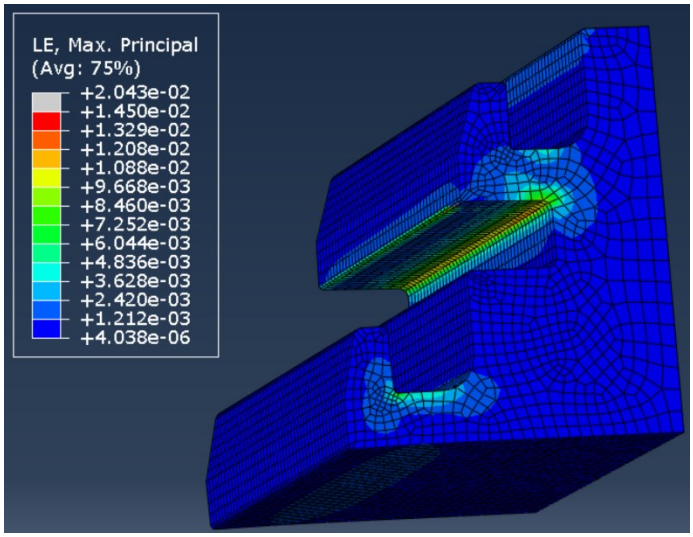

Figure 42 Contour plot of the principal logarithmic strains within the underlapping connector at a displacement of 15.17 mm

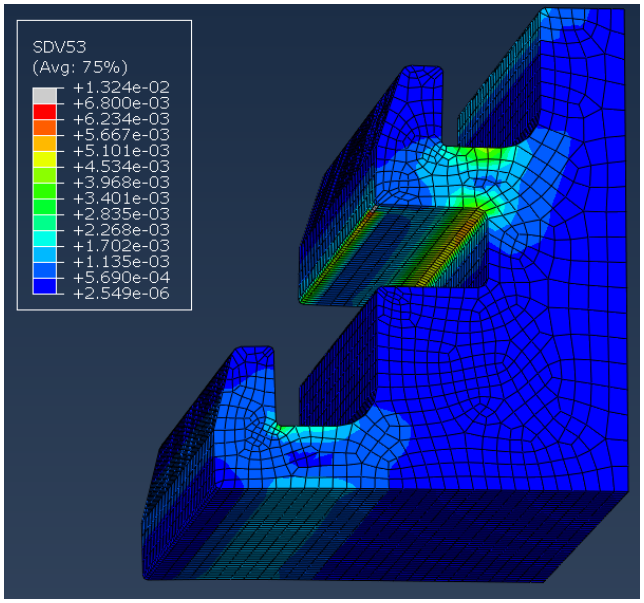

Figure 43 Snapshot of the effective strain amplitude contour plot of the underlapping connector at a 15.17 mm displacement

The predicted total fatigue life was found to be a minimum of 1,122 cycles and located within the upper tooth, which can be seen in Figure 44a-b. The resultant 1,122 cycles is approximately a 1% difference from the 1,132 laboratory-scale data and a 6% difference from the full-scale data determined by Rushing et al. [7,8]. The DMG-MSF model predicted an INC (SDV 58) life of 1,070 cycles and a MSC/PSC (SDV 59) life of approximately 52 cycles in the upper tooth of the underlapping connector. Therefore, the INC stage is still the controlling stage of the fatigue life considering that the MSC/PSC stage only increased from 29 to 52 cycles with a reduction in the effective strain amplitude from 1.5E-02 mm/mm to 6.8E-03 mm/mm. Figure 45a and Figure 45b show the contour plots for the INC and MSC/PSC stages, respectively. In summary, reducing the effective strain amplitude in the connection exponentially increases the INC stage of the fatigue life. Once the maximum effective strain amplitude surpassed 6.8E-03 mm/mm, the total fatigue life rapidly diminished.

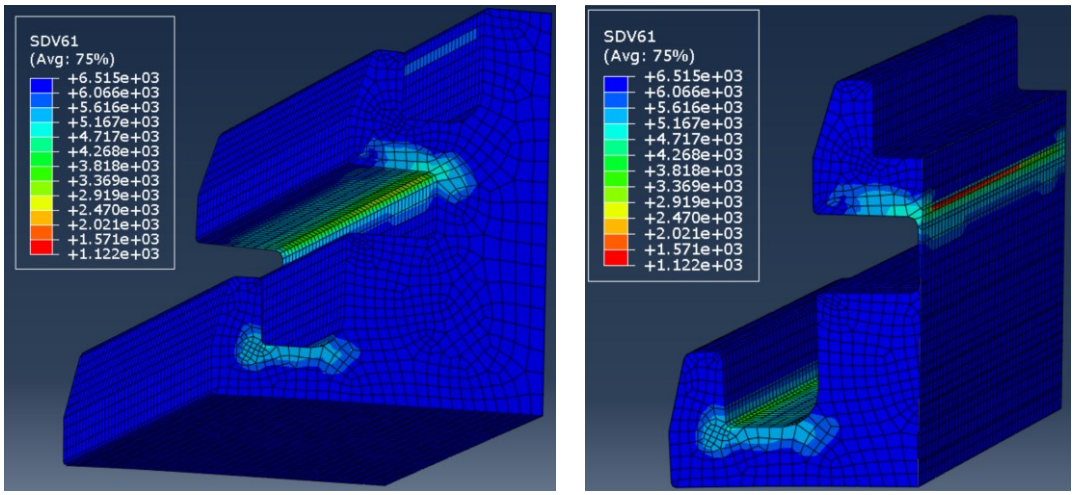

Figure 44 Fatigue life contour plots of the underlapping connector at a displacement of 15.17 mm

Section a) shows the underside of the upper tooth and b) shows an internal view of the upper tooth within the underlapping connector at a maximum displacement of 15.17 mm

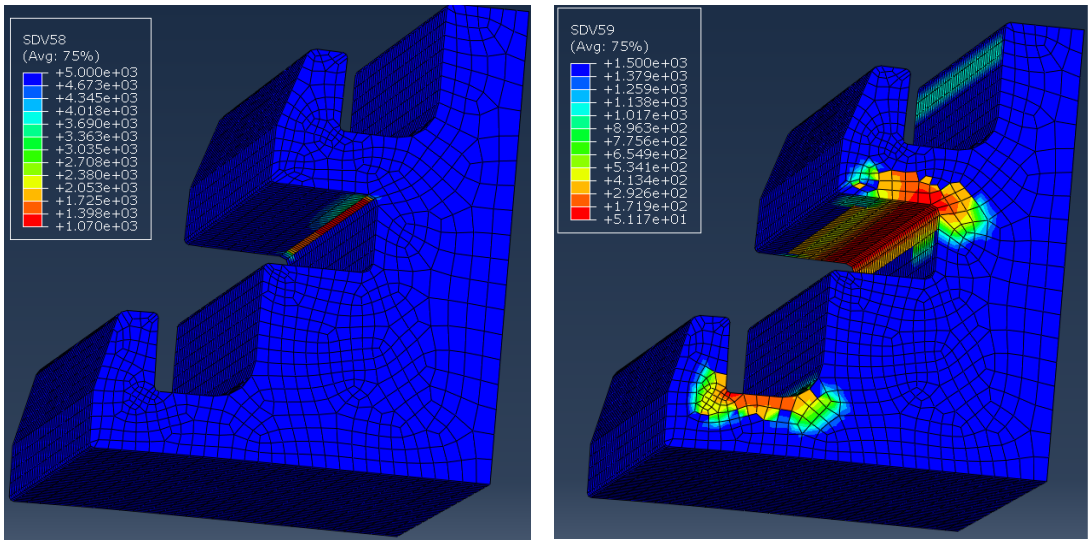

(a) (b)

Figure 45 Contour plots of the INC and MSC/PSC stages at a displacement of 15.17 mm

Section a) shows the INC stage and b) displays the MSC/PSC stage within the underlapping connector

The accurate fatigue life prediction from the DMG-MSF model and correct failure location from the FEM shows that the constant 15.17 mm displacement range characterizes the increasing displacement loading of actual AM2 matting, which is plotted in Figure 46 It should be noted, however, that this characterization only applies to matting over a 6% CBR subgrade. Since the subgrade strength dictates the amount of displacement that occurs in the connection, a subgrade of different strength would have a different characteristic displacement. Even so, the location of the outermost rollers in the FEM should not have to be modified since the rut width in the subgrade is dependent on the traffic application instead of the soil strength. The inner roller on the left hand, or overlapping, side would not have to be modified to test the same connection. If a different connection geometry is being studied, it is suggested to recalibrate the boundary conditions to

verify that the joint has the proper stiffness to mimic the stiffness of the AM2 matting multi-hollow core.

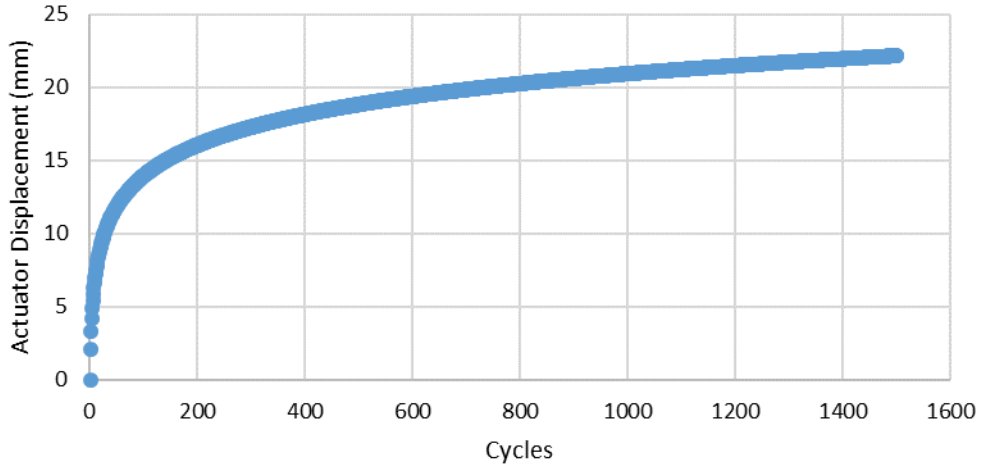

Figure 46 Plot of the actuator displacement versus the number of cycles for the laboratory testing of the AM2 connectors for a subgrade with a strength of CBR 6%

Plot generated from [8,9]

One important thing to consider concerning the repeatability of this FEM is that the DMG-MSF model is designed for constant amplitude fatigue loadings. The loading conditions of AM2 matting present a unique challenge because the matting sees an increasing amplitude displacement controlled by the interaction of the mat system with the subgrade. Figure 46 shows the applied displacement to the joint versus cycle number from the laboratory testing. Therefore, the effective strain amplitude at cycle 1,132 is not representative of the constant strain amplitude that the DMG-MSF model was written for. In the lab, the connection was brought back to its original zero-load position before beginning the next cycle. Since the minimum load applied was zero, the load ratio for the FEM model would be referred to as R=0, where R is equal to the minimum load divided

by the maximum load. Since the AM2 loading cycle only applies a tensile strain, the mean strain and mean stress are greater than zero, which can significantly reduce the fatigue life in aluminum alloys [10]. In contrast, the DMG-MSF material model was calibrated with fully-reversed (R=-1) fatigue data with a mean stress of zero, therefore the calibration did not fit the boundary conditions of the FEM perfectly. Additionally, the DMG model parameters specifically were not calibrated to account for the extruded properties of AA6061-T6, which could have contributed to the error within the single element model calibration.

Potential error was introduced into the model in ways in addition to the physical boundary conditions. Mass scaling was used within the analysis to shorten computational time. Figure 47 shows the kinetic energy versus the internal energy of the model throughout the simulation. The kinetic energy recorded a negligible value compared to internal energy, therefore, the mass scaling used within the simulation had minimal effects on the results, however, it was still a potential error source.

One final consideration regarding error within this model is the actual geometry of the parts. The connection is designed with a large amount of tolerance to be forgiving of subgrade inconsistencies during installation. The large tolerances also mean that the connection could engage differently each cycle, which is why the laboratory testing [7] used rollers instead of fixed supports. The FEM utilized roller constraints as well, however, the engagement of only one cycle was taken into consideration.

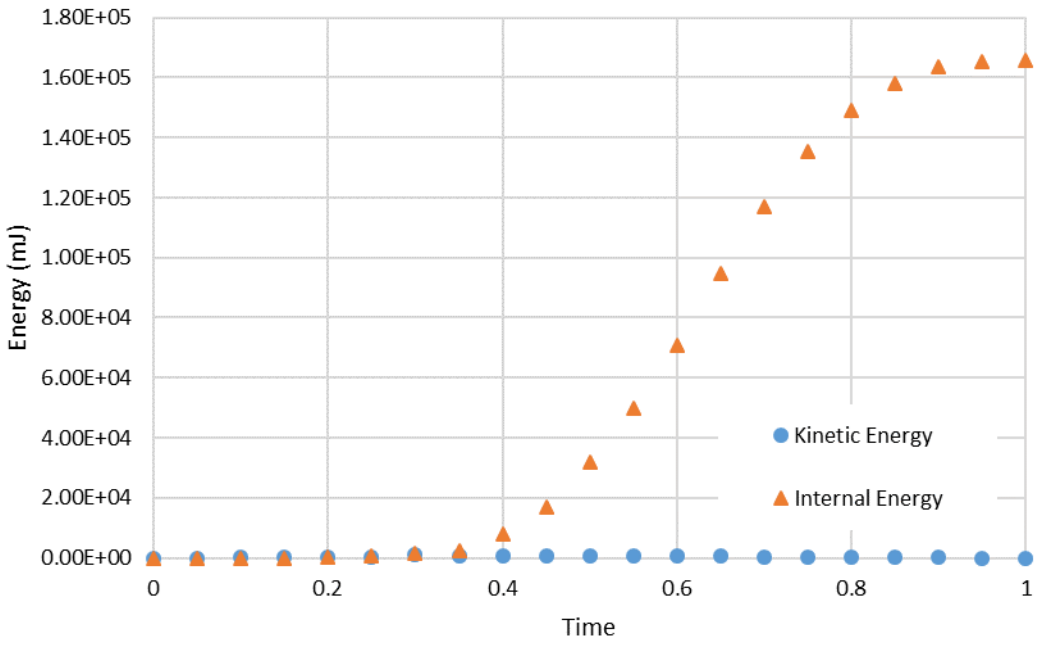

Figure 47 Plot of the internal and kinetic energy plotted versus time for the FEM

In addition to designed tolerances, manufacturing tolerances also have an impact on the fatigue life of the connection. Each side of the connector was modeled as a 2-in. section of the hollow-core extrusion, like was tested in the lab by [7]. Even so, AM2 matting is a multi-hollow-core extrusion and it is assumed that there are measurable differences in wall thickness between each hollow-core depending on its location. Additionally, the location of the extrusion re-weld seams within the hollow-core was not taken into consideration. Finally, the degradation of material properties due to the fusion weld bonding the end connector to the core was not taken into consideration. The dimensional differences between cores, the location of the weld seams, and the weld properties should not have a significant effect on the performance of the actual connector considering that it is extruded separately and the areas of high strain were within the teeth of the connector.

CHAPTER V

CONCLUSIONS

In conclusion, the finite element model in conjunction with the DMG-MSF user-defined material model herein was successfully able to characterize the performance of the extruded AA6061-T6 locking connection of AM2 matting. Extruded AA6061-T6 has microstructural differences from other forms of AA6061-T6 that result in different LCF properties, but the DMG-MSF user-defined material model was able to accurately characterize the material within the LCF realm. A 3D single element model was used to calibrate the DMG-MSF material model prior to implementation into the actual FEM being studied. The DMG-MSF model used the effective strain amplitude to calculate the number of cycles for the INC, MSC/PSC, and LC stages of fatigue life for the connection system. The FEM produced a fatigue life of approximately 11 and 165 cycles to failure for the lower and upper tooth of the underlapping connector, respectively, at the maximum specified displacement of 21.32 mm. The fatigue life results at a displacement of 21.32 mm did not line up with the laboratory- and full-scale data, however, it was not expected to do so.

The DMG-MSF model employs a constant strain amplitude approach while the AM2 matting connection receives an increasing strain amplitude throughout its life due to subgrade deformation below the mat. A characteristic constant displacement range of 15.17 mm was determined for the extruded AA6061-T6 AM2 connection to produce the same fatigue life as the laboratory- and full-scale data. The FEM was evaluated at a maximum displacement of 15.17 mm and produced a fatigue life within 1% of the laboratory-scale data and 6% of the full-scale data at

1,122 cycles. The location of the minimum fatigue life was in the upper tooth of the underlapping connector. It was also noted that the crack incubation was the controlling stage of the total fatigue life, which decreased exponentially as the effective strain amplitude increased. The MSC/PSC regime showed a linear increase and the LC regime remained at zero cycles as the effective strain amplitude decreased.

REFERENCES

[1] Agarwal, H., Gokhale, A. M., Graham, S., & Horstemeyer, M. F. (2003). Void growth in 6061-aluminum alloy under triaxial stress state. Materials Science and Engineering A, 341(1–2), 35–42. https://doi.org/10.1016/S0921-5093(02)00073-4.

[2] Abood, A. N., Saleh, A. H., & Abdullah, Z. W. (2013). Effect of Heat Treatment on Strain Life of Aluminum Alloy AA 6061. Journal of Materials Science Research, 2(2), 51–59. https://doi.org/10.5539/jmsr.v2n2p51.

[3] Badaruddin, M., Zulhanif, & Supriadi, H. (2019). Low Cycle Fatigue Properties of Extruded 6061-T6 Aluminum Alloy. *Journal of Physics: Conference Series*, *1198*(3). https://doi.org/10.1088/1742-6596/1198/3/032002.

[4] Brammer, A. T., Jordon, J. B., Allison, P. G., & Barkey, M. E. (2013). Strain-controlled low-cycle fatigue properties of extruded 6061-T6 aluminum alloy. *Journal of Materials Engineering and Performance*, *22*(5), 1348–1350. https://doi.org/10.1007/s11665-012-0411-0.

[5] McCullough, R. R., Jordon, J. B., Allison, P. G., Rushing, T., & Garcia, L. (2019). Fatigue crack nucleation and small crack growth in an extruded 6061 aluminum alloy. *International Journal of Fatigue*, *119*, 52–61. https://doi.org/10.1016/j.ijfatigue.2018.09.023.

[6] Garcia, L., Rushing, T. W., Mason, Q., Tingle, J. S., & Rutland, C. A. (2015). *AM2 Mat End Connector Modeling and Performance Validation Geotechnical and Structures Laboratory*. (August).

[7] Rushing, T. W., Howard, I. L., Jordon, J. B., & Allison, P. G. (2016). Laboratory characterization of fatigue performance of AM2 aluminum airfield matting. *Journal of Materials in Civil Engineering*, *28*(11), 1–9. https://doi.org/10.1061/(ASCE)MT.1943-5533.0001620.

[8] Rushing, T. W. (2018). Performance Prediction Relationships for AM2 Airfield Matting Developed from Full-Scale Accelerated Testing and Laboratory Experimentation. ERDC/GSL TR-18-1. Vicksburg, MS: U.S. Army Engineer Research and Development Center.

[9] Rushing, T. W., and I. L. Howard. 2017. Analysis of AM2 airfield matting performance under six-wheel Boeing C-17 gear loading. *Journal of Testing and Evaluation,* 45(6). (DOI: 10.1520/JTE20160255).

[10] Stephens, R.I., A. Fatemi, R.R. Stephens, and H.O. Fuchs, Metal Fatigue in Engineering, 2nd ed., John Wiley & Sons, New York, 2001, p 93–121.

[11] Dorward, R. C., & Bouvier, C. (1998). A rationalization of factors affecting strength, ductility and toughness of AA6061-type Al-Mg-Si-(Cu) alloys. *Materials Science and Engineering A*, *254*(1–2), 33–44.

[12] Ozturk, F., Sisman, A., Toros, S., Kilic, S., & Picu, R. C. (2010). Influence of aging treatment on mechanical properties of 6061 aluminum alloy. *Materials and Design*, *31*(2), 972–975. https://doi.org/10.1016/j.matdes.2009.08.017.

[13] Buha J., Lumley R.N., Crosky A.G., Hono K. Secondary precipitation in an Al–Mg–Si–Cu alloy. Acta Mater 2007;55:3015–24.

[14] Takahashi, Y., Shikama, T., Yoshihara, S., Aiura, T., & Noguchi, H. (2012). Study on dominant mechanism of high-cycle fatigue life in 6061-T6 aluminum alloy through microanalyses of microstructurally small cracks. Acta Materialia, 60(6–7), 2554–2567. https://doi.org/10.1016/j.actamat.2012.01.023.

[15] Mccullough, R. R. (2014). *Microstructure-sensitive Plasticity and Fatigue Modeling of Extruded 6061 Aluminum Alloys*. 1–71. (Thesis). The University of Alabama, Tuscaloosa, AL.

[16] Mirza FA, Liu K and Chen XG 2017 Cyclic stress-strain behavior and low cycle fatigue life of AA6061 aluminum alloy. In: Ratvik AP (ed.) Light Metals 2017. *The Minerals, Metals & Materials Series.* Springer, pp. 447-452.

[17] Basquin, O.H. The Exponential Law of Endurance Tests, Am. Soc. Testing Mater. Proc., 1910, 10, p 625–630.

[18] Tavernelli, J.F. and L.F. Coffin, Jr., Experimental Support for Generalized Equation Predicting Low Cycle Fatigue, Trans. ASME, J. Basic Eng, 1962, 84, p 533-536.

[19] Manson, S.S. Discussion of Reference 15, Trans. ASME, J. Basic Eng, 1962, 84, p 537.

[20] Bannantine, J.A., J.J. Comer, and J.L. Handrock, Fundamentals of Metal Fatigue, 1997 (New Jersey) Prentice Hall, 1997 p 40-88.

[21] Wong, W.A., R.J. Bucci, R.H. Stentz, and J.B. Conway, Tensile and Strain-Controlled Fatigue Data for Certain Aluminum Alloys for Application in the Transportation Industry, *Society of Automotive Engineers*, 1987, SAE Technical Paper No. 870094, 16 pp.

[22] Tucker, M. T., Horstemeyer, M. F., Whittington, W. R., Solanki, K. N., & Gullett, P. M. (2010). The effect of varying strain rates and stress states on the plasticity, damage, and fracture of aluminum alloys. *Mechanics of Materials*, *42*(10), 895–907. https://doi.org/10.1016/j.mechmat.2010.07.003.

[23] Bammann, D.J., Chiesa, M.L., Horstemeyer, M.F, and Weingarten, L.I., (1993), Failure in ductile materials using finite element methods, in: N. Jones, T. Weirzbicki (Eds.), Structural Crashworthiness and Failure, Elsevier, Amsterdam, p. 1.

[24] Bammann, D.J., Chiesa, M.L., and Johnson, G.C., (1996), "Modeling Large Deformation and Failure in Manufacturing Process," *Int. J. Solids Struct. in: T*. Tatsumi, E. Wannabe, T. Kambe (Eds.), pp. 256.

[25] Horstemeyer, M.F., Lathrop, J., Gokhale, A.M., Dighe, M.: Modeling stress state dependent damage evolution in a cast Al–Si–Mg aluminum alloy. Theor. Appl. Fract. Mech. 33, 31–47 (2000).

[26] McDowell D. An engineering model for propagation of small cracks in fatigue. Engineering Fracture Mechanics, l 997;56:357-77.

[27] McDowell D. Multiaxial small fatigue crack growth in metals. *International Journal of Fatigue,* 1997;19:127-35.

[28] McDowell, D. L., Gall, K., Horstemeyer, M. F., & Fan, J. (2003). Microstructure-based fatigue modeling of cast A356-T6 alloy. Engineering Fracture Mechanics, 70(1), 49–80. https://doi.org/10.1016/S0013-7944(02)00021-8.

[29] Xue, Y., McDowell, D. L., Horstemeyer, M. F., Dale, M. H., & Jordon, J. B. (2007). Microstructure-based multistage fatigue modeling of aluminum alloy 7075-T651. *Engineering Fracture Mechanics*, *74*(17), 2810–2823. https://doi.org/10.1016/j.engfracmech.2006.12.031.

[30] Xue, Y., El Kadiri, H., Horstemeyer, M. F., Jordon, J. B., & Weiland, H. (2007). Micromechanisms of multistage fatigue crack growth in a high-strength aluminum alloy. *Acta Materialia*, 55(6), 1975–1984. https://doi.org/10.1016/j.actamat.2006.11.009.

[31] Rodriguez, R. I., Jordon, J. B., Allison, P. G., Rushing, T., & Garcia, L. (2016). Low-cycle fatigue of dissimilar friction stir welded aluminum alloys. *Materials Science and Engineering A*, *654*, 236–248. https://doi.org/10.1016/j.msea.2015.11.075.

[32] Cisko, A. R., Jordon, Brian, Rodriguez, Rogie, Rao, Harish, and Allison, P. G. Microstructure-Sensitive Fatigue Modeling of Friction Stir Welded Aluminum Alloy 6061. *Proceedings of the ASME 2015 International Mechanical Engineering Congress and Exposition*. Volume 14: 2015. V014T11A003. ASME. https://doi.org/10.1115/IMECE2015-52307.

[33] Jordon, J.B., J.B. Gibson, M.F. Horstemeyer, H. El Kadiri, J.C. Baird, and A.a. Luo. 2011. "Effect of Twinning, Slip, and Inclusions on the Fatigue Anisotropy of Extrusion-Textured AZ61 Magnesium Alloy." Materials Science and Engineering: A 528 (22-23) (August): 6860–6871. doi:10.1016/j.msea.2011.05.047. http://linkinghub.elsevier.com/retrieve/pii/S092150931100596X.

[34] Hayhurst, D. R., F. A. Leckie, and McDow. 1985. "Damage Growth under Nonproportional Loading." In Multiaxial Fatigue - STP853, 553–558.

[35] Brown, Donald W., A. Jain, Sean R. Agnew, and Bjørn Clausen. 2007. "Twinning and Detwinning during Cyclic Deformation of Mg Alloy AZ31B." Materials Science Forum 539-543: 3407–3413. doi:10.4028/www.scientific.net/MSF.539-543.3407. http://www.scientific.net/MSF.539-543.3407.

[36] Kumai, S, JE King, and JF Knott. 1990. "Short and Long Fatigue Crack Growth in a SiC Reinforced Aluminium Alloy." Fatigue & Fracture of Engineering Materials & Structures 13 (5): 511–524. http://onlinelibrary.wiley.com/doi/10.1111/j.1460-2695.1990.tb00621.x/abstract.

[37] Newman, J.C. 1995. "Fatigue-Life Prediction Methodology Using a Crack-Closure Model." Journal of Engineering Materials and Technology 117 (4): 433–439.

[38] Paris, P.C., Gomez, M.P., and Anderson, W.E., (1961), "A rational analytic theory of fatigue," he Trend in Engineering, Vol. 13: pp. 9–14.

[39] Jordon, J.B., M.F. Horstemeyer, N. Yang, J.F. Major, K.a. Gall, J. Fan, and D.L. McDowell. 2009. "Microstructural Inclusion Influence on Fatigue of a Cast A356 Aluminum Alloy." Metallurgical and Materials Transactions A 41 (2) (November 4): 356–363. doi:10.1007/s11661-009-0088-7. http://www.springerlink.com/index/10.1007/s11661-009-0088-7.

[40] Rettberg, Luke H., J. Brian Jordon, Mark F. Horstemeyer, and J. Wayne Jones. 2012. "Low-Cycle Fatigue Behavior of Die-Cast Mg Alloys AZ91 and AM60." Metallurgical and Materials Transactions A 43 (7) (March 22): 2260–2274. doi:10.1007/s11661-012-1114-8. http://www.springerlink.com/index/10.1007/s11661-012-1114-8.